Experimental investigation of vortex-induced vibration of a flexible pipe in bidirectionally sheared flow

Xuepeng Fu [a,b,c], Shixiao Fu [a,b,c,*], Haojie Ren [a,b,c], Wenhui Xie [d], Yuwang Xu [a,b,c], Mengmeng Zhang [a,b,c], Zhenhui Liu [e], Shuai Meng [a,b,c]

[a] *State Key Laboratory of Ocean Engineering, Shanghai Jiao Tong University, Shanghai, 200240, China*
[b] *Collaborative Innovation Centre for Advanced Ship and Deep-Sea Exploration, Shanghai, 200240, China*
[c] *Institute of Polar and Ocean Technology, Institute of Marine Equipment, Shanghai Jiao Tong University, Shanghai, 200240, China*
[d] *CNOOC Research Institute Limited, Beijing, 100028, China*
[e] *Aker Solutions AS, Ranheimsveien 10, Trondheim 7044, Norway*

ARTICLE INFO

ABSTRACT

The existence of a bidirectionally sheared flow field caused by internal solitary waves has recently been confirmed according to a field survey in the South China Sea. A model test of a tensioned flexible pipe in bidirectionally sheared flow was performed in an ocean basin. The model was 28.41 mm in diameter and 7.64 m in length. The purpose of the model test was to understand the response performance and obtain benchmark data of vortex-induced vibration (VIV) in bidirectionally sheared flow. The test was performed on a rotating test rig to simulate bidirectionally sheared flow conditions. Fiber Bragg Grating (FBG) strain sensors were arranged along the test pipe to measure bending strains, and the modal analysis approach was used to determine the VIV response. Reduced velocities based on the tested first natural frequency in water reached 30.79. The cross-flow and in-line VIV amplitudes, response frequencies in statistics and time-domain analysis, traveling wave characteristics, phase synchronization and trajectories are presented in this article. The maximum root mean square (RMS) VIV amplitudes in the test reached 0.51 diameters and 0.18 diameters in the cross-flow and in-line directions, respectively. A relative low Strouhal number of 0.10 was found in the CF direction.

© 2022 Elsevier Ltd. All rights reserved.

1. Introduction

Slender flexible structures in ocean engineering, such as risers and pipelines, are affected by alternating vortex shedding caused by ocean currents. These vortices will induce such structures to oscillate in the in-line (IL) and cross-flow (CF) directions, which are called vortex-induced vibration (VIV). VIV has been confirmed as a significant factor of fatigue damage and may magnify the drag forces of risers. These issues have been widely studied over 5 decades, and many reviews have been published: Vandiver (1993), Trim et al. (2005), Chaplin et al. (2005a), Willden and Graham (2001), Tognarelli et al. (2004), Williamson and Govardhan (2004), Sarpkaya (2004), Williamson and Govardhan (2008) and Wu et al. (2012).

Self-oscillation tests of rigid pipes in steady flow were conducted first to investigate VIV. The vibrations in the only CF and IL-CF combined directions were studied. Many critical parameters and phenomena have been proposed and identified,
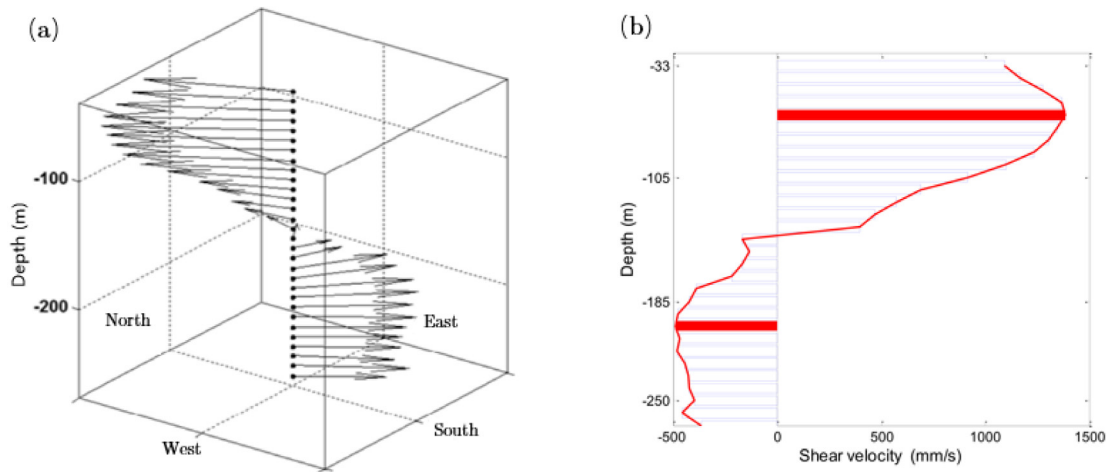

Fig. 1. The shear currents profile of internal solitary waves. (a) current vector diagram (from Xie et al., 2018); (b) current velocity profile (from Xie and Lei, 2013).

enriching our fundamental knowledge of VIV (Jauvtis Na and Williamson, 2004; Williamson and Roshko, 1988; Govardhan and Williamson, 2000). However, VIV of flexible structures is characterized by multimode and multifrequency vibrations which are different from the rigid pipe. VIV of flexible pipes under different kinds of current profiles has been studied in recent years. One of the most systematic researches towards the VIV of flexible pipes is the joint industry project (JIP) of Norwegian Deepwater Program (NDP). NDP (Vikestad et al., 2000) has performed a series of VIV experiments on flexible risers in uniform flow and linearly sheared flow. Based on experimental results, many empirical prediction models have been proposed and revised, such as SHEAR7 (Vandiver et al., 2005), VIVANA (Larsen et al., 2001) and VIVA (Triantafyllou et al., 1999). These models are designed to solving engineering problems such as VIV response prediction.

In the South China Sea, a special flow field induced by internal solitons exists. Xie et al. (2018) at the CNOOC Research Institute performed a six-month field survey in the Liuhua area of the South China Sea. The current speed characteristics of internal solitons are shown in Fig. 1. A special flow profile was found to have nearly opposite flow directions, asymmetrical velocity values, and a sheared distribution in the region near 185 m in depth. The internal solitons induced flow usually occurs with internal soliton waves which occur on average 62 times per month and last about 18 min during each occurrence based on the field survey report (Xie et al., 2018) which suggests that this flow field affects the risers for 18.6 h every month on average. And its impact on flexible pipe VIV behavior has not been investigated. Due to the limitation of the ocean basin dimension, it is impractical to simulate such a flow field in laboratory. We simplify this flow field as a *bidirectionally sheared flow* with perfectly opposite flow directions, symmetry velocity values, and a sheared distribution, which is different from the linearly sheared flow investigated in previous experiments, to preliminary study of VIV characteristics in this particular flow field.

Currently, VIV experiments of slender pipes in bidirectionally sheared flow have not been performed, and benchmark data for empirical prediction models are lacking. A Joint Industry Project (JIP) project, Flow Induced Force and its Effects on Risers and Subsea Structures (FIFERS), is established and aims to propose a VIV prediction model for complex flow fields including bidirectionally sheared flow. As an important aspect of this project, a model test of a tensioned flexible pipe in bidirectionally sheared flow is performed. The model is 28.41 mm in diameter and 269 diameters in length. The reduced velocities based on the tested first natural frequency in water reach 30.79. The benchmark data, including cross-flow and in-line VIV amplitudes; response frequencies in statistics and time-domain analysis; traveling wave characteristics; trajectories; and phase synchronization in bidirectionally sheared flow, are represented.

Hopefully, these experimental results will provide some guidelines for VIV prediction and industry.

2. Experimental set-up

2.1. Test apparatus

A model test was performed in an ocean basin at Shanghai Jiao Tong University. The experimental apparatus, which contains the rotating rig and flexible pipe model, is installed on the false bottom of the basin, as shown in Figs. 2 and 3. The effective current profile creates a bidirectionally sheared distribution. During the experiment, the driven wheel moves at the same given linear velocity motivated by the servo motor. The test pipe model is installed on two sides through the diameter of the driven gear, which is equipped with clamps, U-joints and a force sensor which is also used in Ren et al. (2019). The distance from the false bottom to the experimental pipe is 26D. The force sensor is connected to a tensioner fixed on the driven gear. A pretension force of 980 N is applied to the pipe model through the tensioner.
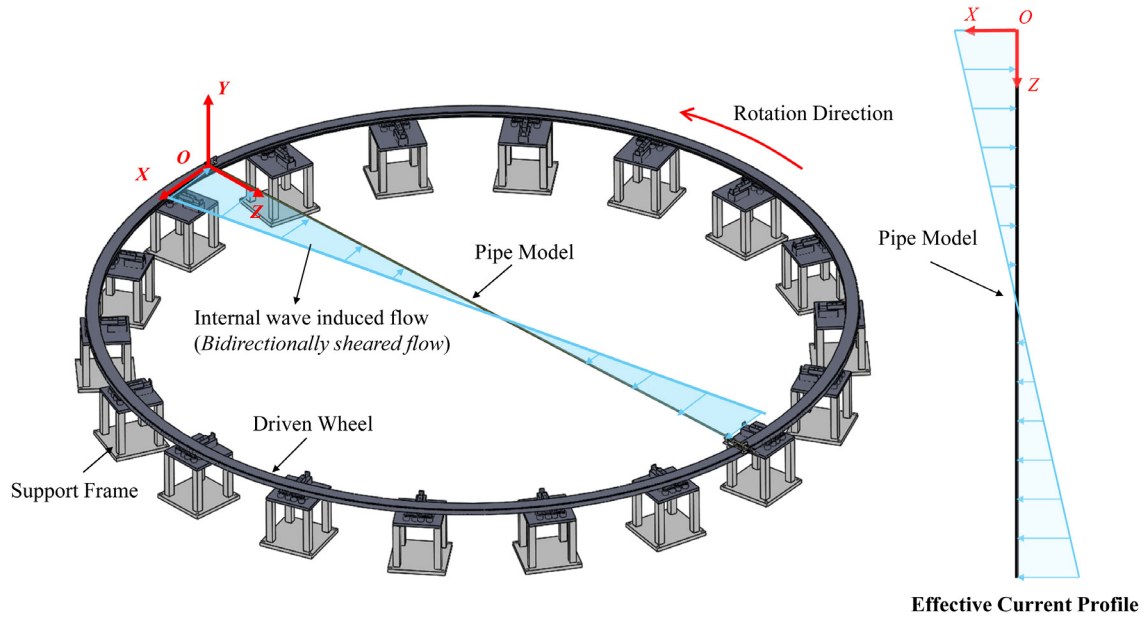
Fig. 2. Sketch of experiment apparatus. (For interpretation of the references to color in this figure legend, the reader is referred to the web version of this article.)
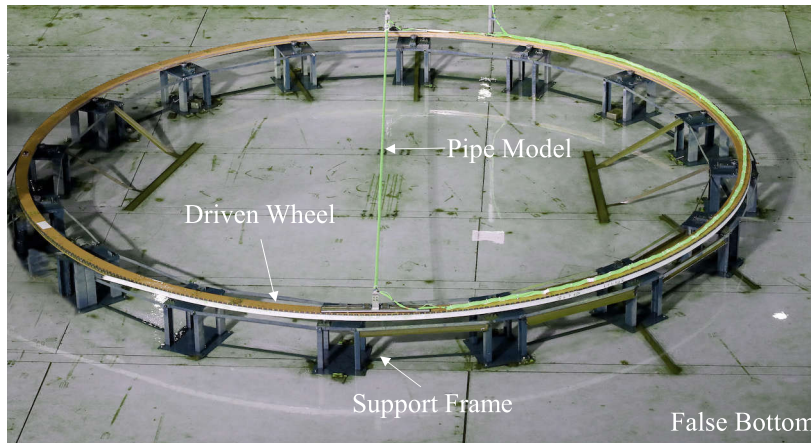

Fig. 3. Overview of the experimental set-up.

The pipe model is primarily created with an external polypropylene random copolymer (PPR) pipe and an internal copper cable. Silicone rubber is applied between different layers to avoid relative sliding.

The coordinate system is defined as O-XYZ, as shown in Fig. 2. The origin(O) is set at one ending point of the pipe model without the tensioner. The X-, Y- and Z- axes are along the in-line (IL), cross-flow (CF) and axis of the test pipe model. The rotation direction during the experiment is always along the X-axis and the effective current profile is shown with colors and arrows. The maximum flow velocity U_{max} is the equivalent flow velocity at the origin of the coordinate.

The primary physical properties of the test pipe model are listed in Table 1. The first three tested natural frequencies are obtained by a free decay experiment, and the calculated 1st natural frequency in water is calculated by Eq. (1). The theoretical value of the 1st natural frequency differs from the experimentally measured value by 5%.

$$f_{cn} = \frac{n^2\pi}{2}\sqrt{\left(1 + \frac{L^2 T_0}{n^2\pi^2 EI}\right)\frac{EI}{\bar{m}'L^4}}, \quad \bar{m}' = \bar{m} + \frac{1}{4}C_m\rho\pi D^2 \; (C_m = 1.00) \quad (n = 1, 2, 3\ldots) \tag{1}$$

Table 1
Physical properties of the test pipe model.

| Parameter	Value of test model
Pipe model length L (m)	7.64
Outer diameter D (mm)	28.41
Mass in air $\bar{m}$ (kg/m)	1.24
Pretension T_0 (N)	980
Bending stiffness EI (N m^2)	58.6
Tensile stiffness EA (N)	9.4E5
Damping ratio ζ (%)	2.58
Tested 1st natural frequency in water f_{n1} (Hz)	1.59
Tested 2nd natural frequency in water f_{n2} (Hz)	3.14
Tested 3rd natural frequency in water f_{n3} (Hz)	4.78
Calculated 1st natural frequency in water f_{cn1} (Hz)	1.51
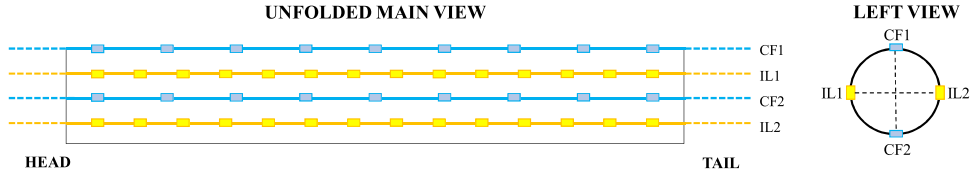
Fig. 4. Locations of FBG strain sensors along test pipe model.

where T_0 is the pretension; $\bar{m}$ and $\bar{m}'$ are the mass per unit length in air and still water, respectively; D, L and EI are the diameter, length and bending stiffness of the test pipe model, respectively; ρ is the density of water, and $\rho = 1000\,\text{kg/m}^3$; and the added mass coefficient C_m is set as 1.00.

As shown in Fig. 4, a total of 46 Fiber Bragg Grating (FBG) strain sensors in four groups are installed along the test pipe to measure dynamic strains in both the IL and CF directions. The FBG strain sensors are placed on the surface PPR cylinder with $D_{PPR} = 25.00$ mm, and a coating is covered to protect the fiber sensors. The strains described below are strains on the surface of the coating calculated by multiplying the measured strains by D/D_{PPR}. The head is the origin of the coordinate. The gaps among the groups of CF strain sensors (CF1 and CF2) and IL strain sensors (IL1 and IL2) are approximately 65.00 mm and 45.5 mm, respectively, as shown in Fig. 4. The strains along the pipe model are synchronously recorded at a sampling frequency of 250 Hz.

2.2. Test condition

During the experiment, the maximum flow velocity U_{max} varied from 0.30 to 1.39 m/s with a total of 58 test conditions. The corresponding reduced velocity Vr ($Vr = U_{max}/(D \cdot f_{n1})$) value range is 6.59 to 30.79. To obtain sufficient strain information for analysis, the test pipe rotates one circle per test. The VIV during the second half circle is affected by the turbulence induced by that of the first half circle. The analysis of this problem will be discussed in the Section 4.

3. Data analysis

3.1. Preprocessing

A pretension of 980 N is applied at the test pipe model, but the tension is varied under the effect of the drag force, which will yield variable axial strain. Thus, the measured strain at the sensor location in the CF direction $\varepsilon_{CF}(z, t)$ contains three parts: the initial axial strain ε_{T0} induced by pretension, the variable axial strain $\varepsilon_T(t)$ caused by varying tension, and the bending strain $\varepsilon_{VIV}(z, t)$ caused by VIV. The strain at z locations of CF1 and CF2 can therefore be written as:

$$\varepsilon_{CF1}(z, t) = \varepsilon_{T0} + \varepsilon_T(t) + \varepsilon_{CF-VIV}(z, t) \tag{2}$$

$$\varepsilon_{CF2}(z, t) = \varepsilon_{T0} + \varepsilon_T(t) - \varepsilon_{CF-VIV}(z, t) \tag{3}$$

Combining Eqs. (2) and (3), the CF VIV strain at the z location can be calculated by:

$$\varepsilon_{CF-VIV}(z, t) = \left[\varepsilon_{CF1}(z, t) - \varepsilon_{CF2}(z, t)\right]/2 \tag{4}$$

Since IL VIV is a periodic process with a mean value of zero, the time averaged value of the IL-VIV strain equals zero:

$$\overline{\varepsilon_{IL-VIV}(z, t)} = 0 \tag{5}$$

Also, the initial bending strain does not vary with time and can be expressed as:

$$\varepsilon_{initial}(z) = \overline{\varepsilon_{IL}(z,t)} \tag{6}$$

Combining the above formulae, the initial bending strain and IL VIV strain can be derived as:

$$\varepsilon_{initial}(z) = \overline{[\varepsilon_{IL1}(z,t) - \varepsilon_{IL2}(z,t)]}/2 \tag{7}$$

$$\varepsilon_{IL-VIV}(z,t) = \left[\varepsilon_{IL1}(z,t) - \varepsilon_{IL2}(z,t) - \overline{\varepsilon_{IL1}(z,t) - \varepsilon_{IL2}(z,t)}\right]/2 \tag{8}$$

It should be noted that the VIV strains in this paper are strains on the surface of the coating calculated by

$$\varepsilon_{VIV}(z,t) = \varepsilon_{VIV,m}(z,t) \cdot \frac{D}{D_{PPR}} \tag{9}$$

where the $\varepsilon_{VIV,m}(z,t)$ is the VIV strains calculated from the measured strains.

Bandpass filtering is applied to the strain signal to eliminate unavoidable noise. The high-pass and low-pass cutoffs are 0.8 Hz and 20 Hz, respectively.

3.2. Modal analysis method

The VIV displacement in the IL and CF directions can be obtained by the modal analysis method through measured IL and CF VIV strain.

The modal analysis method assumes that the VIV displacement can be expressed as a sum of modal shapes multiplied by the modal weights at each time step. The VIV displacement in the CF direction can be expressed as:

$$y(z,t) = \sum_{i=1}^{n} p_i(t)\varphi_i(z), \quad z \in [0,L] \tag{10}$$

where $y(z,t)$ is the VIV displacement in the CF direction at the z location, $p_i(t)$ is the ith modal weight of the displacement at time t, and $\varphi_i(z)$ is the ith modal shape of the displacement at z location.

Based on the small deformation assumption, the curvature $\kappa(z,t)$ can be derived from the displacement modal shape as:

$$\kappa(z,t) = \frac{\partial^2 y(z,t)}{\partial z^2} = \sum_{i=1}^{n} p_i(t)\varphi_i''(z), \quad z \in [0,L] \tag{11}$$

where $\varphi''(z)$ is the ith modal weight of the curvature. Based on the relationship between curvature and strain, we have:

$$\varepsilon(z,t) = \kappa(z,t)R = R\sum_{i=1}^{n} p_i(t)\varphi_i''(z), \quad z \in [0,L] \tag{12}$$

where $R = D/2$ is the radius of the pipe model.

For the test pipe model, the modal shapes of displacement can be treated as the modal shape of the beam pinned at both ends, which can be expressed as:

$$\varphi_i(z) = \sin\frac{i\pi z}{L}, \quad i = 1, 2 \cdots \tag{13}$$

The modal shapes of curvature $\varphi''(z)$ are also sinusoidal and the strain can be calculated by:

$$\varepsilon(z,t) = -R\sum_{i=1}^{n}\left(\frac{i\pi}{l}\right)^2 p_i(t)\varphi_i(z), \quad z \in [0,L] \tag{14}$$

where $\varepsilon(z,t)$ is the VIV bending strain. Then the modal weight of the displacement $p_i(t)$ can be obtained through Eq. (14) and the VIV displacement in the CF direction can be derived directly using Eq. (10). The derivation of VIV displacement in the IL direction $x(z,t)$ follows similarly.

The modes used for reconstructing displacement in modal analysis (Eq. (10)) are selected in the present study since low modes are very sensitive to measurement noise in VIV experiment (Lie and Kaasen, 2006). Here, we set a threshold with a value of 10% of the maximum curvature RMS weight of different modes, and the modes in which modal weights are larger than this value will be employed for displacement reconstruction. The modes for displacement reconstruction are chosen separately for each test. A similar way of choosing modes for the response reconstruction is referred to Huera-Huarte (2006).

In addition, the initial mean bending strain and the initial bending displacement $x_{initial}(z)$ induced by the mean drag force follow the relationship:

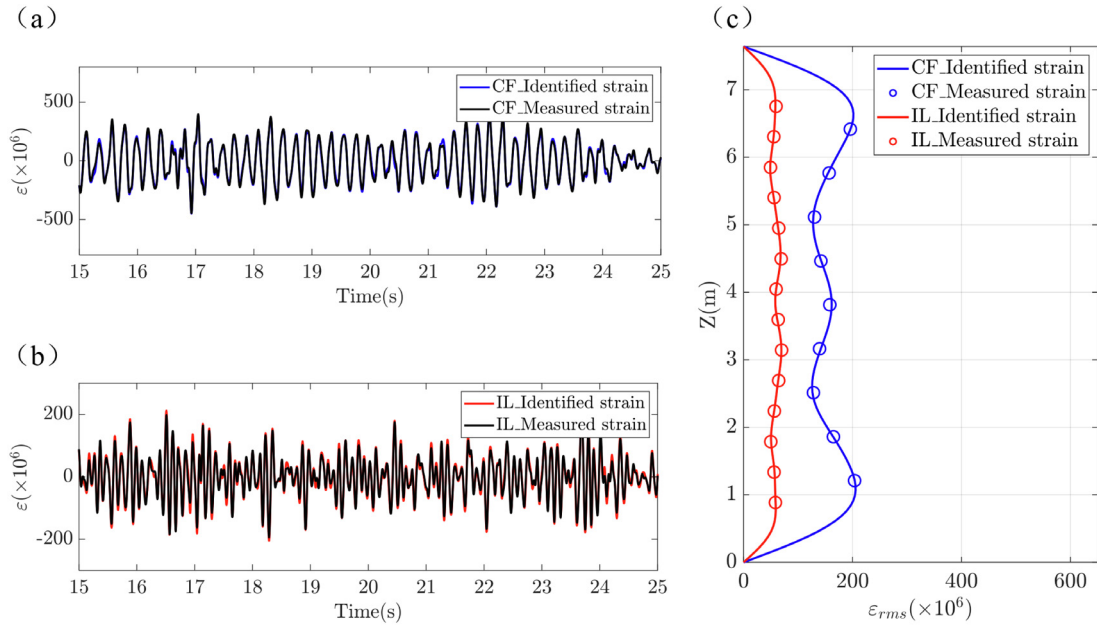$$\varepsilon_{initial}(z) = R\frac{\partial^2 x_{initial}(z)}{\partial z^2} \tag{15}$$

Fig. 5. Comparison between the identified and measured strain in the case $U_{max} = 1.19\,\text{m/s}$: (a) time histories of identified and measured strain in the CF direction at the 5th sensor point ($z = 3.81\,\text{m}$); (b) time histories of identified and measured strain in the IL direction at the 7th sensor point ($z = 3.60\,\text{m}$); (c) distribution of root mean square of VIV strain along the test pipe model. (For interpretation of the references to color in this figure legend, the reader is referred to the web version of this article.)

Base on Eq. (15), the initial bending displacement $x_{initial}(z)$ can also be obtained by the modal analysis method.

The feasibility of the modal analysis method in the VIV test under bidirectionally sheared flow is evaluated in the present study. The measured strain is compared with the identified strain which is derived by the second order difference of the identified displacement. Fig. 5 shows the comparison result of the identified and measured strain under $U_{max} = 1.19\,\text{m/s}$. As shown in Fig. 5(a) and (b), the identified CF and IL strains are in good agreement with the measured strain in the time domain. In Fig. 5(c), the blue and red lines are the identified strains in the CF and IL directions, respectively. The red and blue circles represent the measured strain in the CF and IL directions, respectively. The distribution of the identified strain along the pipe matches well with the measured strain. This result demonstrates the applicability of the modal analysis method toward VIV of flexible pipes under bidirectionally sheared flow.

3.3. Time–frequency analysis

To investigate the time–frequency feature of the VIV response under bidirectionally sheared flow, wavelet transformation is used. The continuous wavelet transform equation is expressed as:

$$WT_f(a, \tau) = \langle f(t), \psi_{a,\tau}(t) \rangle = a^{-1/2} \int_{-\infty}^{+\infty} f(t)\psi^* \left(\frac{t - \tau}{a} \right) dt \tag{16}$$

where WT_f is the wavelet transformation coefficient of the time domain signal $f(t)$, which represents the variation in frequency at that time scale. Parameter a is the scale factor, τ is the shift factor, $\psi(t)$ is the mother wavelet, and the Morlet wavelet is chosen as the mother wavelet.

4. Credibility analysis

Compared with the VIV experiment apparatus for other steady flow conditions in previous studies, the VIV experiment apparatus for bidirectionally sheared flow introduced in this article contains complex mechanical transmission devices, and the credibility is analyzed through the following aspects:

1. To obtain sufficient VIV strain information, the test pipe rotates one circle per test. The VIV during the second half-circle is affected by the turbulence induced by that of the first half circle, and the influence of the turbulence is discussed.
2. The time history of VIV is shown to ensure that the experimental data obtained in the experiment can reflect the characteristics of the stable VIV induced by the bidirectionally sheared flow.
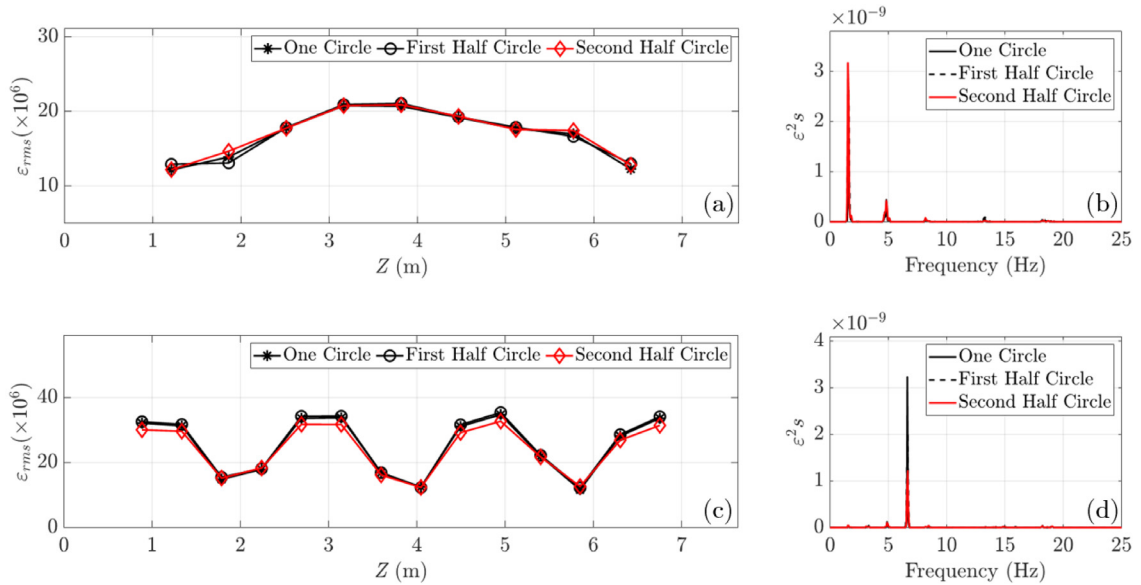
Fig. 6. Comparison of CF strains in the one circle, the first circle and the second half-circle in the case $U_{max} = 0.48$ m/s. (a) root mean square of CF strains at measuring points along the test pipe; (b) power spectral densities of CF strains at the 5th sensor point ($z = 3.81$ m); (c) root mean square of IL strains at measuring points along the test pipe; (d) power spectral densities of IL strains at the 7th sensor point ($z = 3.60$ m).

3. The experimental data under four different water depths (distance from water surface to the false bottom of ocean basin, WD) are tested and compared to confirm that the experimental data were not affected by the water depth and to determine the experimental water depth.
4. A noise evaluation of air machinery was performed, and it was confirmed that mechanical friction did not affect VIV.
5. Repetitive experiments are set to verify the repeatability of the test results.

4.1. Influence of wake induced by the previous circle

Undoubtedly, it is best to obtain the VIV data in the pure flow field during the test. In this experiment, only the first half circle flow field is pure, but VIV data of the first half circle (nearly 25 periods) are not sufficient for analysis. To obtain sufficient VIV data, the test pipe has to rotate for a full circle. The influence of wake induced by the first half circle is discussed.

The comparison of RMS values of strains at the measuring points in the CF and IL directions, and the power spectral densities of strains at the 5th CF measuring point and 7th IL measuring point in different circles are shown in Fig. 6 for $U_{max} = 0.48$ m/s and in Fig. 7 for $U_{max} = 1.39$ m/s. The data of the first half circle and the second half circle are directly extracted from the data of the first one circle. It should be noted that the $2f_{CF}$ component is not obvious in the IL results since the CF and IL measurement points in the experiment are not symmetrical distributed, and the IL measurement point shown is close to one node of the fourth order.

There are few differences among the RMS values of strain and the peak frequency of the strain power spectral density of different circles. Therefore, the turbulence of the first half circle does not appear to influence VIV response of the second half circle significantly during the first circle. The VIV strains of the first one circle are used for further analysis.

4.2. Time history of VIV

The test pipe cannot rotate too many circles during the experiment due to the effect of the wake induced by the rotation. In this experiment, the test pipe is rotated once to prevent excessive wake influence.

The time series of edge displacement and VIV strains at $U_{max} = 0.67$ m/s and $U_{max} = 1.39$ m/s are given in Figs. 8 and 9. There are three typical phases of initial phase, stable VIV phase, and end phase in the time series of an experimental condition. The displacement of the test pipe edge is shown at the top of the figures, and the red lines represent the stable VIV phase. The time–history strain at the 5th measuring point in the CF direction (FBG-CF5) and the 8th measuring point in the IL direction (FBG-IL8) are shown in the middle and bottom of the figures, respectively. The results show the stable VIV phase reaches nearly 50 and 100 periods, which is sufficient for further analysis.
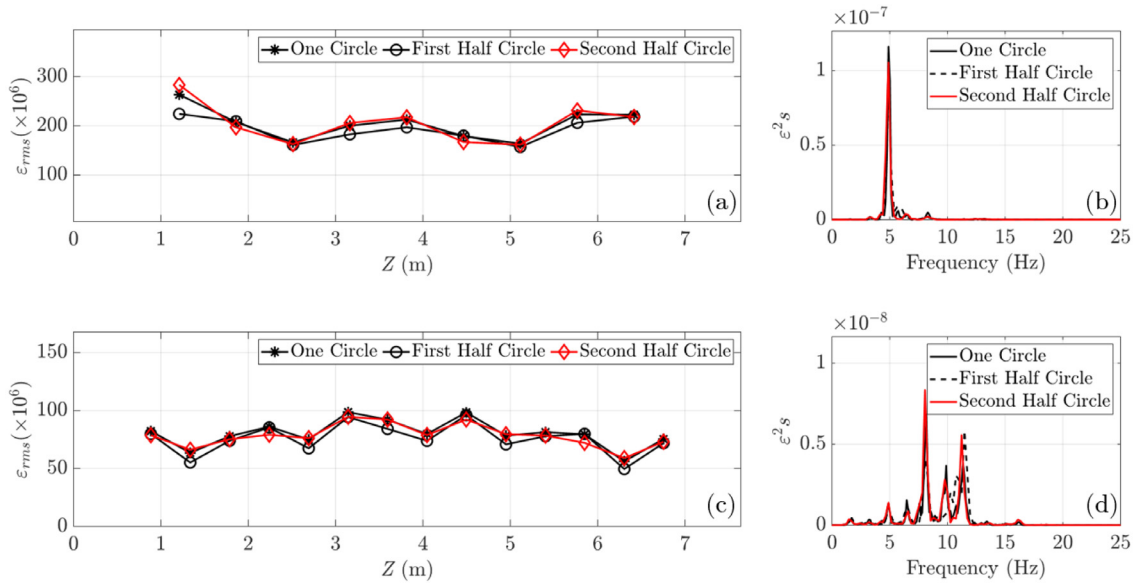
Fig. 7. Comparison of CF strains in the one circle, the first circle and the second half-circle in the case $U_{max} = 1.39$ m/s. (a) root mean square of CF strains at measuring points along the test pipe; (b) power spectral densities of CF strains at the 5th sensor point ($z = 3.81$ m); (c) root mean square of IL strains at measuring points along the test pipe; (d) power spectral densities of IL strains at the 7th sensor point ($z = 3.60$ m).
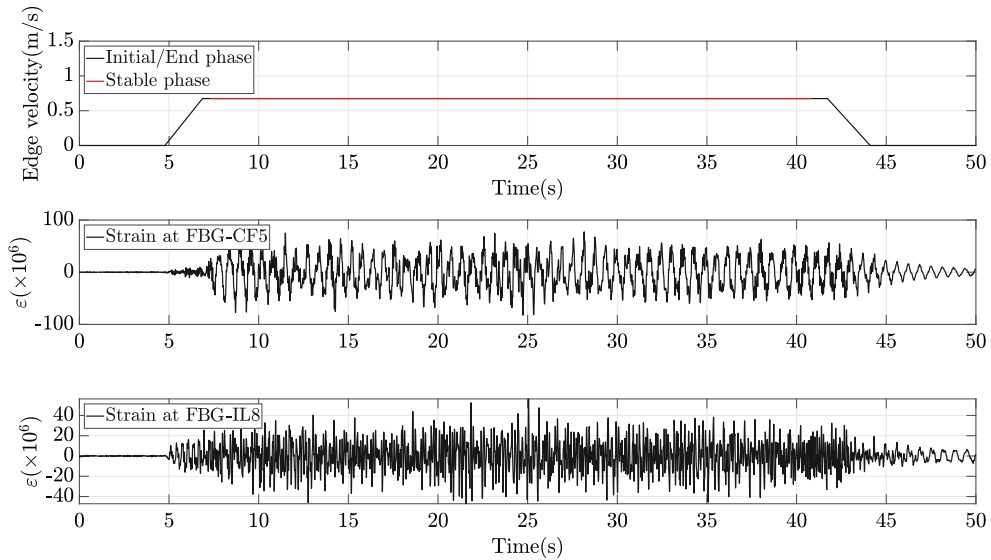

Fig. 8. Time series of edge velocity and VIV strains at $U_{max} = 0.67$ m/s. Top: Velocity of the edge; Middle: Strain signal at the 5th measuring point in the CF direction; Bottom: Strain signal at the 8th measuring point in the IL direction. (For interpretation of the references to color in this figure legend, the reader is referred to the web version of this article.)

4.3. Water depth

In the present study, the test pipe are installed in the driven wheel, the distance between the test pipe and false bottom is 26D. A sketch of experiment apparatus from the side is displayed in Fig. 10. To avoid the effect of free-surface proximity effect, four different water depths ($WD = 1.00$ m, 1.20 m, 1.30 m and 1.40 m) are tested to determine the appropriate experimental water depth. The corresponding distance between the test pipe and free-surface is nearly 9.20D, 16.20D, 19.80D and 23.30D, respectively.

The comparison of RMS values of strains at the measuring points in the CF direction are shown in Fig. 11(a) for $U_{max} = 0.99$ m/s and in Fig. 11(b) for $U_{max} = 1.39$ m/s. The RMS values of strains at different measuring points are calculated by the data of the first one circle. The RMS values of VIV strain do not change greatly when the water depth
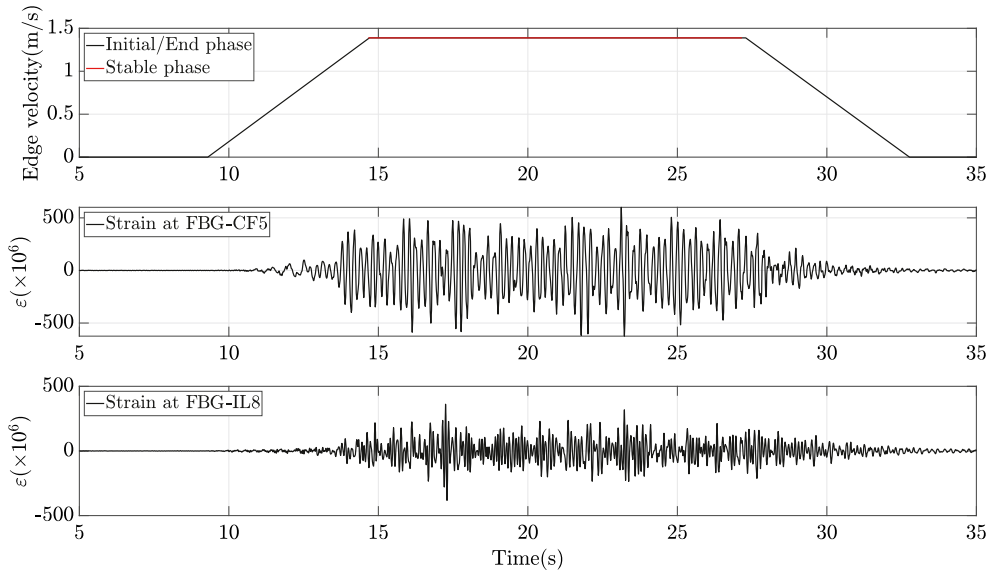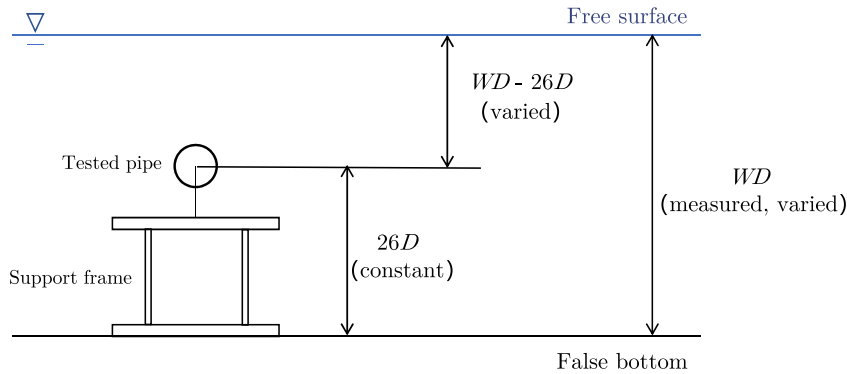
Fig. 9. Time series of edge displacement and VIV strains at $U_{max} = 1.39$ m/s. Top: Velocity of the edge; Middle: Strain signal at the 5th measuring point in the CF direction; Bottom: Strain signal at the 8th measuring point in the IL direction.

Fig. 10. Sketch of experiment apparatus from the side view.

exceeds as shown in the figure. The most conservative water depth of 1.40 m is selected as the formal experimental water depth to avoid free-surface effect.

4.4. Noise signal induced by experiment apparatus

The flow field in this experiment is generated by the rotation of a nearly 8-meter diameter aluminum driven wheel that constantly scrapes the bearing on the support. Therefore, it is inevitable that some noise signals will be generated by the scraping, and it becomes more noticeable as the flow velocity increases. The strain signals in water and air under the maximum flow velocity condition ($U_{max} = 1.39$ m/s) are compared in Fig. 12, where the black and red lines represent the strain signal at FGB-CF5 in water and air, respectively. The strain signals measured in air are assumed to be all noise signals, and the strain signals obtained underwater are the sum of noise signals and VIV signals. These results demonstrate that the noise signal (red line) is less than 1% of the vortex-induced vibration signal (black line), and that the experimental apparatus has nearly no effect on the vortex-induced vibration signal.

4.5. Repetitive experiment

A repetitive experiment of $U_{max} = 0.99$ m/s is planned to boost the credibility of VIV results. The VIV strain and displacement results are shown in Fig. 13. In repetitive experiments, the relative difference of RMS strains of measuring points does not exceed 7%, and nearly identical maximum RMS VIV displacement is achieved. Therefore, the experimental results are repeatable.
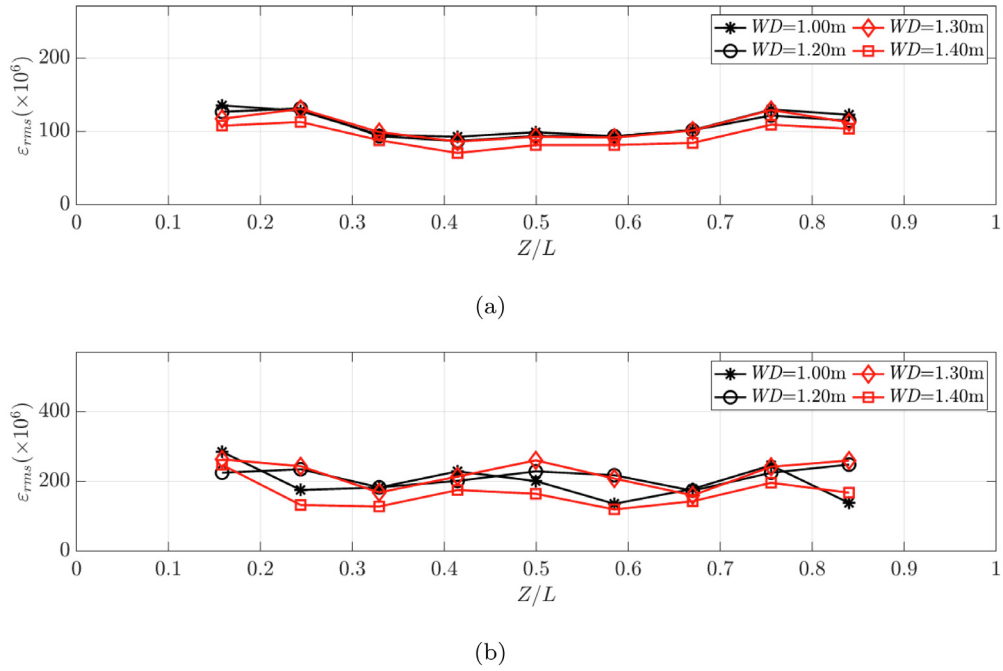
(a)

(b)

Fig. 11. RMS strains at different measuring points in the CF direction under different water depth ($WD = 1.00$ m, 1.20 m, 1.30 m, 1.40 m). (a) $U_{max} = 0.99$ m/s; (b) $U_{max} = 1.39$ m/s.
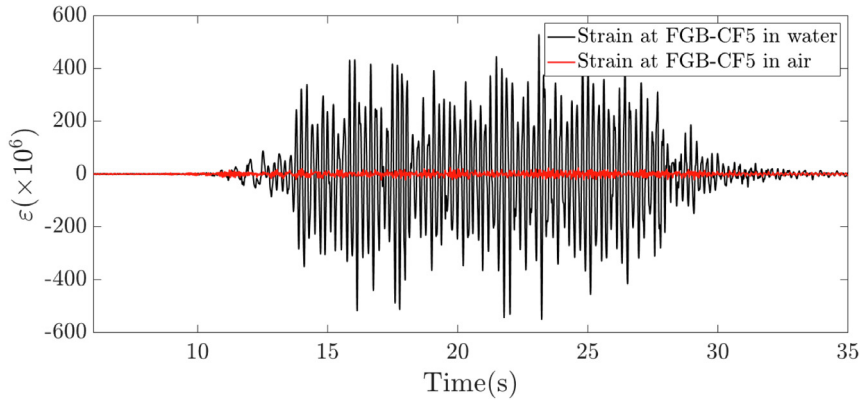

Fig. 12. Time history of strain at FGB-CF5 location at $U_{max} = 1.39$ m/s. Black line: strain signal in water; Red line: strain signal in the air. (For interpretation of the references to color in this figure legend, the reader is referred to the web version of this article.)

5. Results and discussions

5.1. VIV displacement and frequency response

The selected results of initial displacement in the IL direction (A_{ini}), RMS value of VIV displacement (A) and power spectral density (PSD) of displacement along the cylinder are shown in Fig. 14 for $U_{max} = 0.46$ m/s, in Fig. 15 for $U_{max} = 0.48$ m/s, in Fig. 16 for $U_{max} = 0.87$ m/s and in Fig. 17 for $U_{max} = 1.15$ m/s. The subfigure (c) and (d) are the contour plots of PSD of displacement along the cylinder. The initial displacement, as shown in subfigure (a), presents as a distribution that is identical to the 2nd order mode for all tests, which is induced by the current velocity direction profile.

The flexible pipe vibrates at exactly the 1st order in the CF direction and the 2nd order in the IL direction at $U_{max} = 0.46$ m/s as shown in Fig. 14(b),(c), and (d). When the flow velocity increases, the VIV response presents 'multi-frequency' characteristics. The flexible pipe vibrates at exactly the 1st order in the CF direction and combines the 2nd and 4th orders in the IL direction at $U_{max} = 0.48$ m/s (shown in Fig. 15). When U_{max} reaches 0.87 m/s (Fig. 16), the pipe
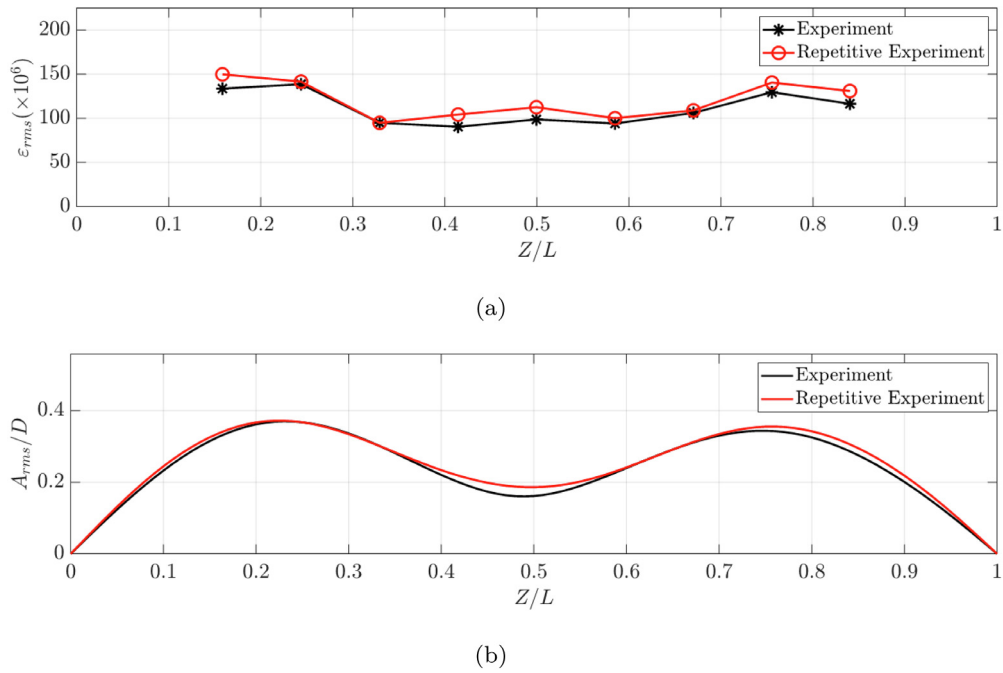
(a)

(b)

Fig. 13. RMS strains at different measuring points and displacement along the test pipe in the CF direction under $U_{max} = 0.99$ m/s. (a): RMS VIV strain; (b): RMS VIV displacement.
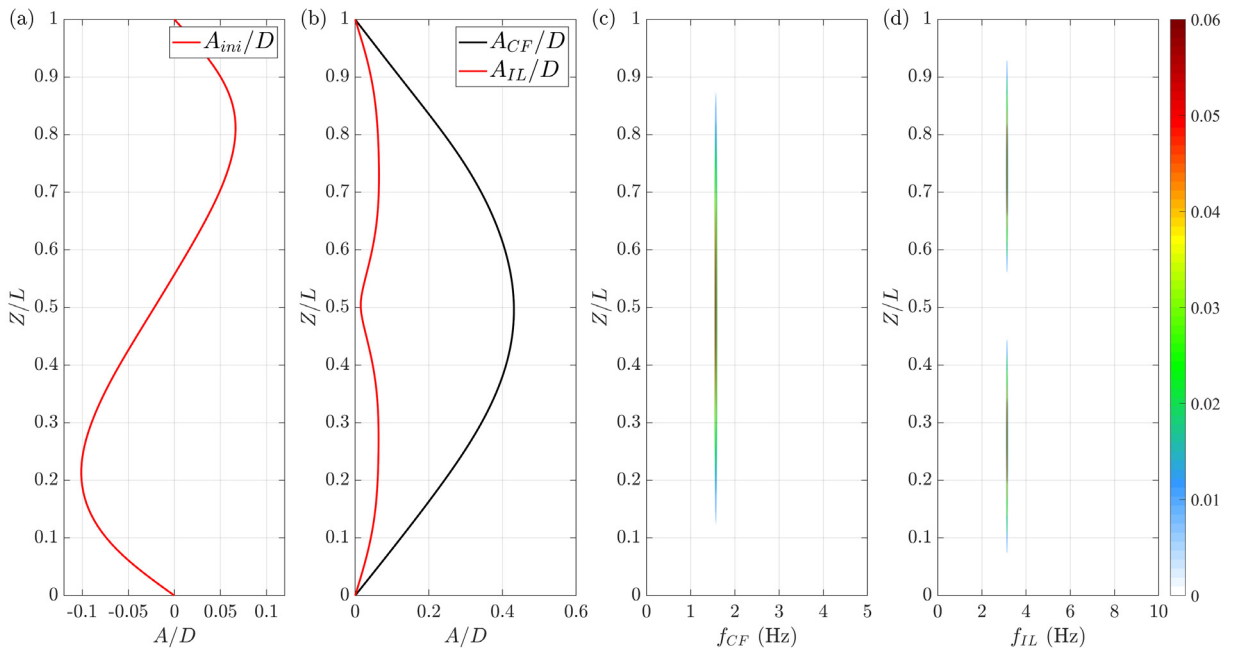

Fig. 14. Spanwise distribution of VIV response at $U_{max} = 0.46$ m/s: (a) initial displacement in the IL direction; (b) VIV RMS displacement in the IL (red) and CF (black) direction; (c) frequency distribution of CF displacement; (d) frequency distribution of IL displacement. (For interpretation of the references to color in this figure legend, the reader is referred to the web version of this article.)

vibrates at combining the 1st and 2nd orders in the CF direction and at combining the 2nd and 4th orders. When the U_{max} reaches 1.15 m/s (Fig. 17), the pipe vibrates at the 2nd and 3rd order in the CF direction and contains multiple frequency components mainly dominated by the 4th order and 5th mode in the IL direction. In general, responses at several frequencies can be observed along the span in bidirectionally sheared flow. Broadband vibration in the range of
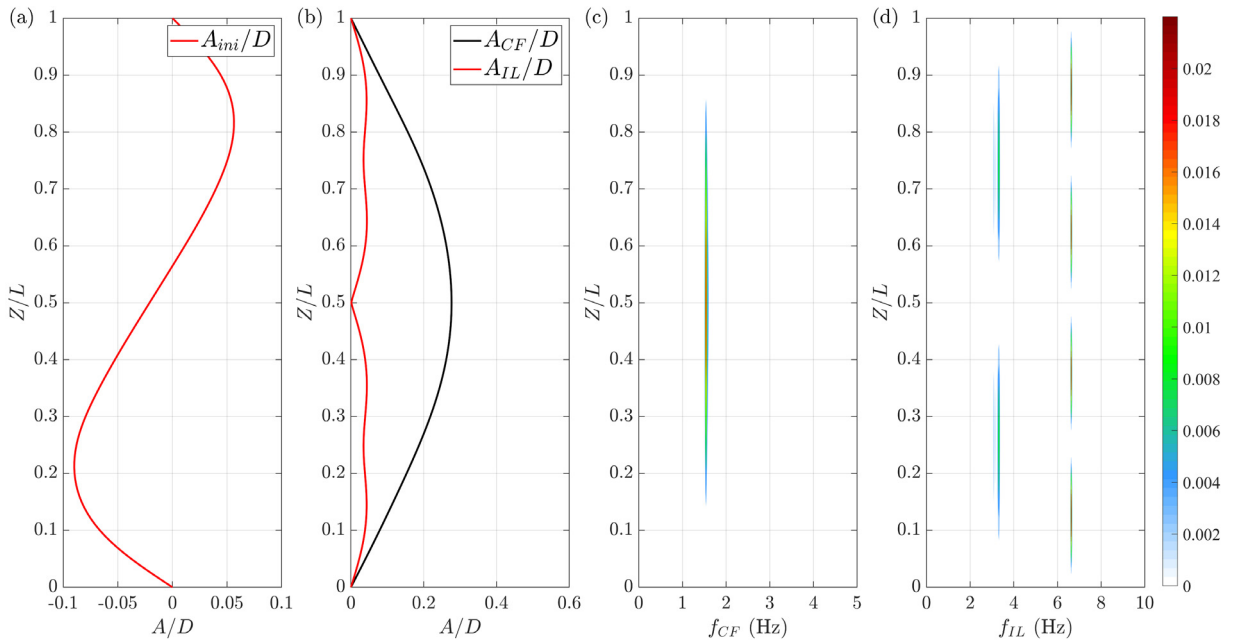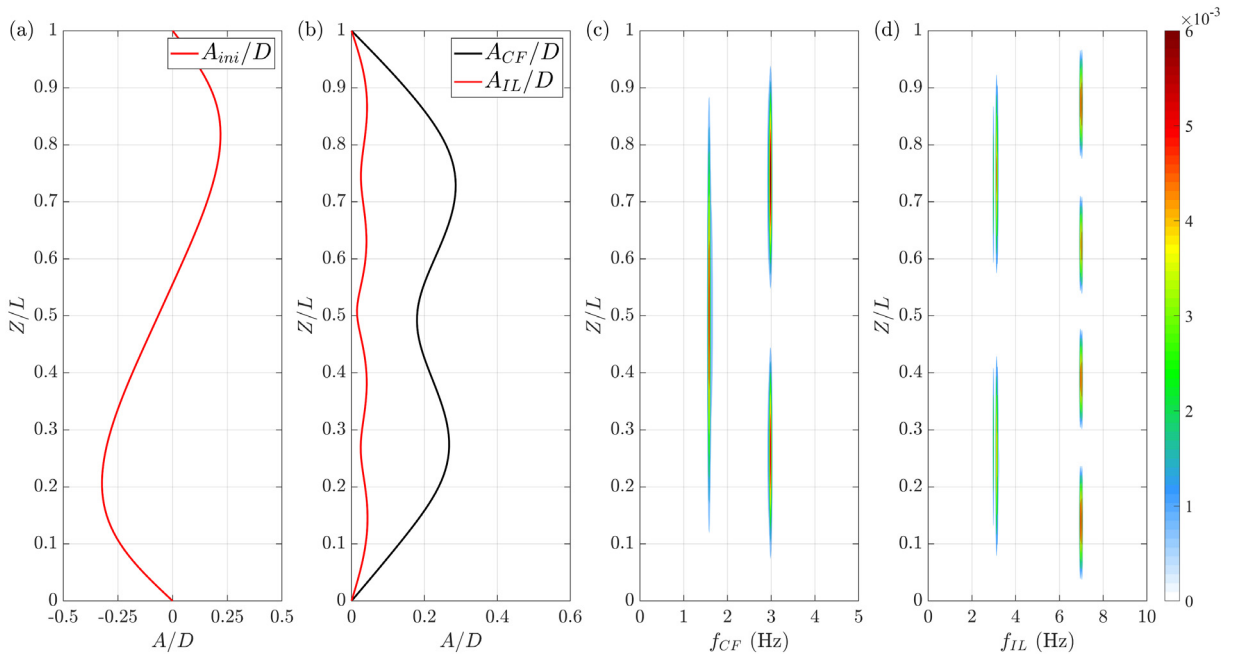
Fig. 15. Spanwise distribution of VIV response at $U_{max} = 0.48$ m/s: (a) initial displacement in the IL direction; (b) VIV RMS displacement in the IL (red) and CF (black) direction; (c) frequency distribution of CF displacement; (d) frequency distribution of IL displacement. (For interpretation of the references to color in this figure legend, the reader is referred to the web version of this article.)

Fig. 16. Spanwise distribution of VIV response at $U_{max} = 0.87$ m/s: (a) initial displacement in the IL direction; (b) VIV RMS displacement in the IL (red) and CF (black) direction; (c) frequency distribution of CF displacement; (d) frequency distribution of IL displacement. (For interpretation of the references to color in this figure legend, the reader is referred to the web version of this article.)

[0, 10] is observed in the IL VIV response, and the odd-order mode (the 3rd mode) is suppressed. The reason why the 3rd mode is suppressed should be the 2nd order similar profile of current velocity enhanced even-order (the 2nd and 4th modes) response. Different from the IL direction, there exists the 3rd mode response at $U_{max} = 1.15$ m/s in the CF
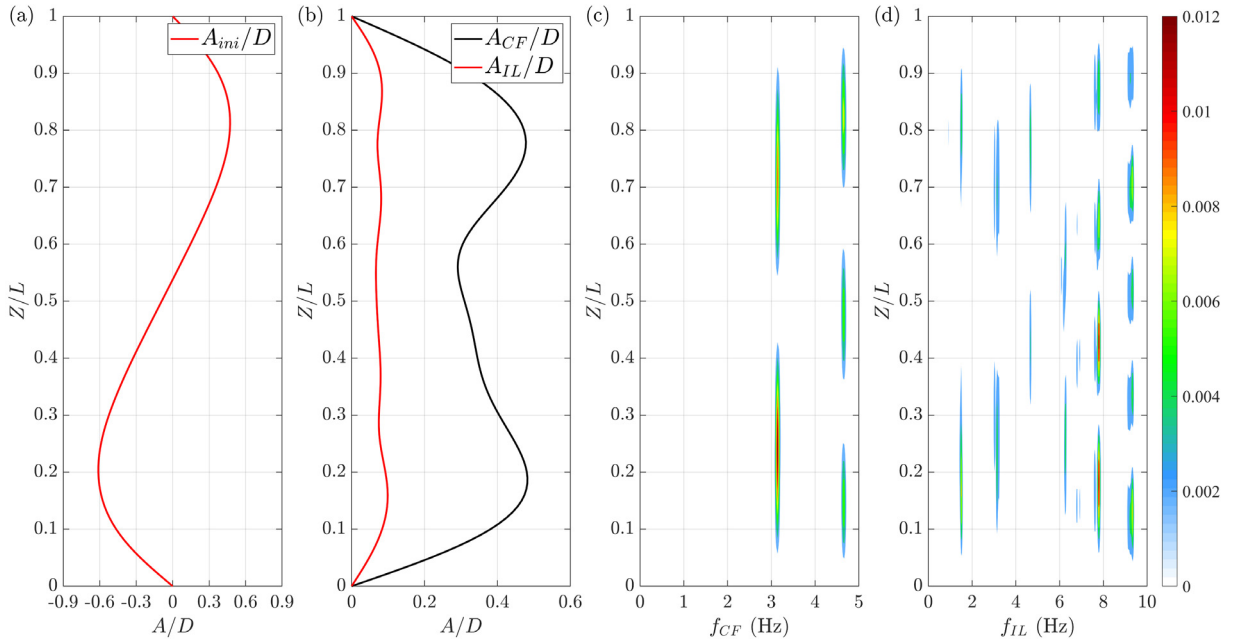
Fig. 17. Spanwise distribution of VIV response at $U_{max} = 1.15\,\text{m/s}$: (a) initial displacement in the IL direction; (b) VIV RMS displacement in the IL (red) and CF (black) direction; (c) frequency distribution of CF displacement; (d) frequency distribution of IL displacement. (For interpretation of the references to color in this figure legend, the reader is referred to the web version of this article.)

direction, which indicates that the profile of current velocity has no marked effect on the response in the CF direction, and the 'multi-frequency' characteristic is also observed.

Based on Figs. 14–17, the maximum RMS VIV amplitudes in the CF and IL directions across the spanwise direction for different Vr are selected and plotted in Figs. 18 and 19. The dominant modes with respect to the curvature (dominant IL mode/dominant CF mode) are marked and grouped with a red dotted line. We can observe the dominant modes in the IL, and the CF direction increases with Vr. The phenomena of displacement dropping when the mode switches and monotonically increasing in a group found in previous studies for linear flow (Trim et al., 2005), linearly sheared flow (Wang et al., 2021) and stepped flow (Chaplin et al., 2005b) are not observed in our experiment. Not only do modal groups '2n/n' and '2n/2n-1' occur during the experiment, but modal groups '3/1' and '4/1' exist when Vr is less than 12 because the current profile may generate a higher IL excitation mode compared with the one-direction flow. Also, the VIV displacement does not switch during mode transitions, and the dominant mode in the IL direction controls the VIV displacement response. The VIV displacement remains constant or decreases marginally when IL VIV is dominated by the even order (e.g., the 4 or 6 order), and increases when the IL VIV is dominated by the odd order (e.g., the 3 or 5 order). The maximum RMS VIV amplitudes in the experiment reach $0.57D$ and $0.11D$ in the CF and IL directions, respectively. The maximum CF VIV response amplitude at $Re > 1E4$ varies at the range of $[0.2D, 0.6D]$, which is basically the same as Swithenbank et al. (2008) found. It should be noted that Re and following St in the present study is based on the maximum flow velocity which is not the best way to represent the bidirectionally sheared flow. The more proper velocity to calculate Re under bidirectionally sheared flow will be investigated in the future (e.g. VIV prediction and hydrodynamic analysis).

To study the characteristic of dominant frequency in bidirectionally sheared flow, the general amplitude–frequency spectrum proposed by Wang et al. (2014) is introduced:

$$F(\omega) = \sum_{i=1}^{n} \hat{f_i}(\omega) \tag{17}$$

where, $\hat{f_i}(\omega)$ is the PSD at the ith measuring point and is a function of strain amplitude with respect to the response frequency. $F(\omega)$ is the general amplitude–frequency spectrum obtained by summing the strain amplitude at the same frequency component for all the measuring points. The dominant frequency is the frequency associated with the peak of the general spectrum. The frequency ratio is defined as f_{domi}/f_{n1}, where f_{domi} is the dominant frequency and f_{n1} is the tested 1st natural frequency.

Figs. 20 and 21 show the frequency ratio of the CF and IL directions against Vr. The dominant frequencies in the CF direction are basically fixed in the first three natural frequencies, and the dominant frequencies in the IL direction are fixed at twice the CF dominant frequency or the nearest natural frequency. In addition, the frequency ratio in both the CF
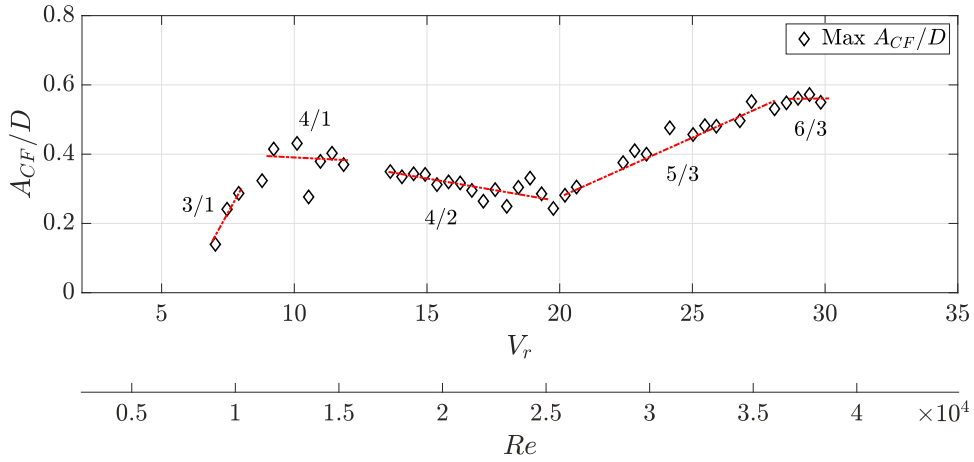
Fig. 18. Maximum RMS amplitude of displacement in the CF direction along the spanwise versus *Vr* and *Re*. Black diamonds indicate the maximum RMS amplitude of the CF displacement. Cases in the same modal group (same dominant mode in the CF and IL directions) are labeled (IL dominant mode/CF dominant mode) together with the red dotted line. (For interpretation of the references to color in this figure legend, the reader is referred to the web version of this article.)
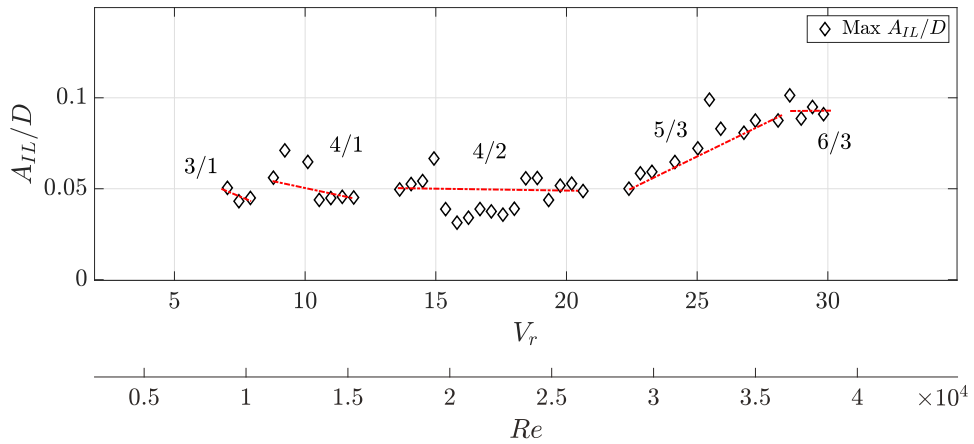

Fig. 19. Maximum RMS amplitude of displacement in the IL direction along the spanwise versus *Vr* and *Re*. Black diamonds indicate the maximum RMS amplitude of the IL displacement. Cases in the same modal group are labeled together with the red dotted line. (For interpretation of the references to color in this figure legend, the reader is referred to the web version of this article.)
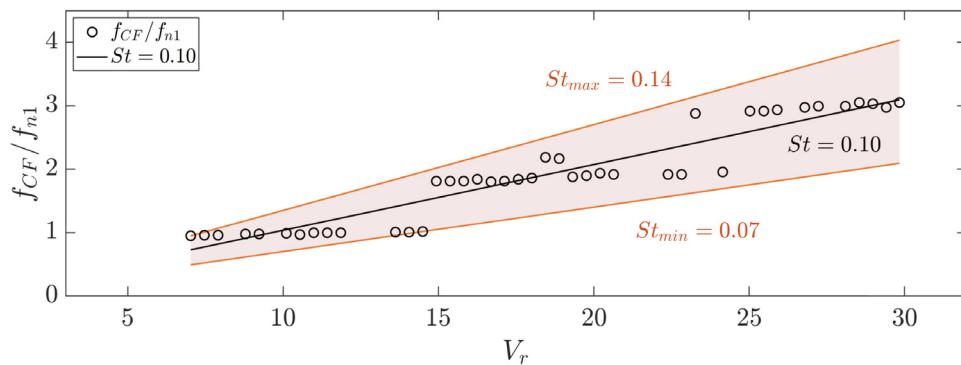
Fig. 20. Frequency ratio of the CF direction against *Vr*. Black circles, CF frequency ratio f_{CF}/f_{n1}; Black line, fitted curve (zero intercept) for CF direction, the slope of the fitted curve is the *St* number; Orange lines, fitted curve (zero intercept) with maximum and minimum *St* number. (For interpretation of the references to color in this figure legend, the reader is referred to the web version of this article.)
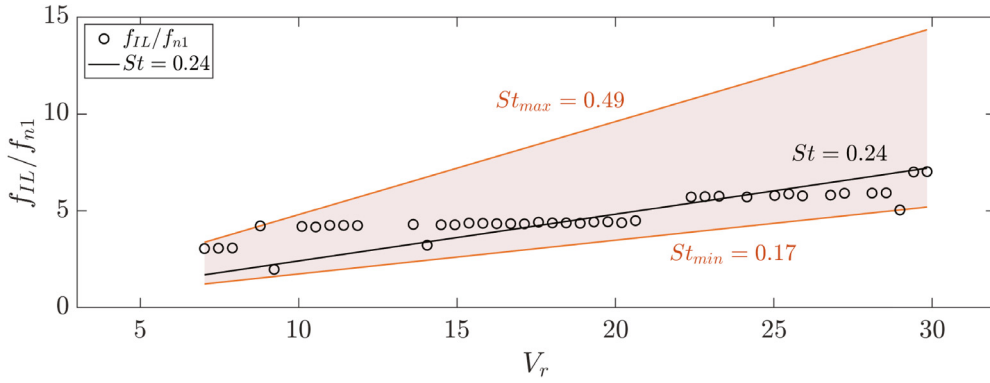
Fig. 21. Frequency ratio of the IL direction against Vr. Black circles, IL frequency ratio f_{IL}/f_{n1}; Black line, fitted curve (zero intercept) for IL direction, the slope of the fitted curve is the St number; Orange lines, fitted curve (zero intercept) with maximum and minimum St number. (For interpretation of the references to color in this figure legend, the reader is referred to the web version of this article.)
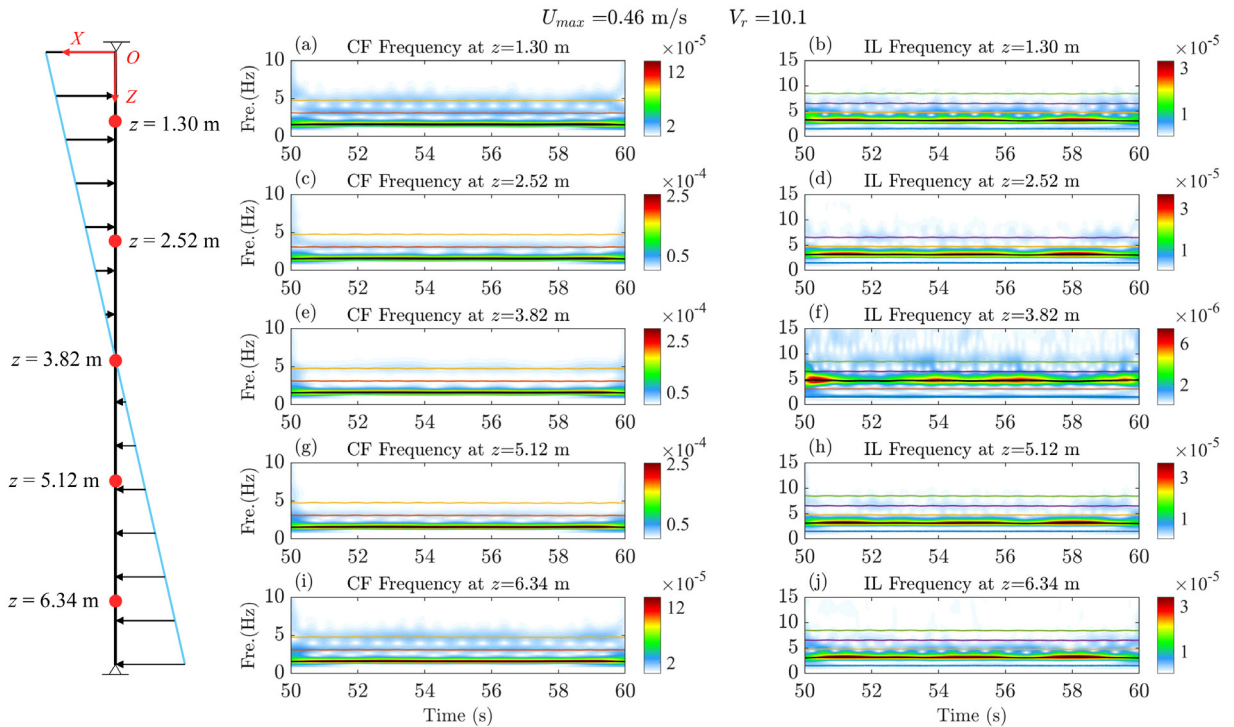
Fig. 22. Time-varying response frequency for case $U_{max} = 0.46$ m/s, $Vr = 10.10$. The left sketch presents the flow profile and probe points (solid red dots); a,c,e,g,i: time-varying CF response frequency at 5 selected probe points, the instantaneous natural frequency of the first three orders based on Eq. (1) are displayed; b,d,f,h,j: time-varying IL response frequency at 5 selected probe points. The instantaneous natural frequency of the selected orders based on Eq. (1) are shown. The black line represents the time-varying dominant frequency. (For interpretation of the references to color in this figure legend, the reader is referred to the web version of this article.)

and IL directions changes stepwise rather than linearly with Vr. The Strouhal number (St) is obtained by the slope of the linear fit line with zero intercept shown in the figure and equals 0.10 and 0.24 in the CF and IL directions, respectively. The St value is smaller than that in uniform flow ($St \approx 0.18$, Gao et al. (2015)) and linearly sheared flow ($St \approx 0.13$, Lie and Kaasen (2006)), which means that a higher flow velocity will activate a smaller VIV response frequency. It should be noted that linear fit is not ideal as the previous research on uniform and linearly sheared flow because the VIV response frequencies in bidirectionally sheared flow are almost locked to the natural frequencies. The orange regions in the figures represent the Strouhal number range based on single experimental data. The bidirectionally sheared flow induced VIV prediction method is about to be implemented to develop a more proper frequency model.
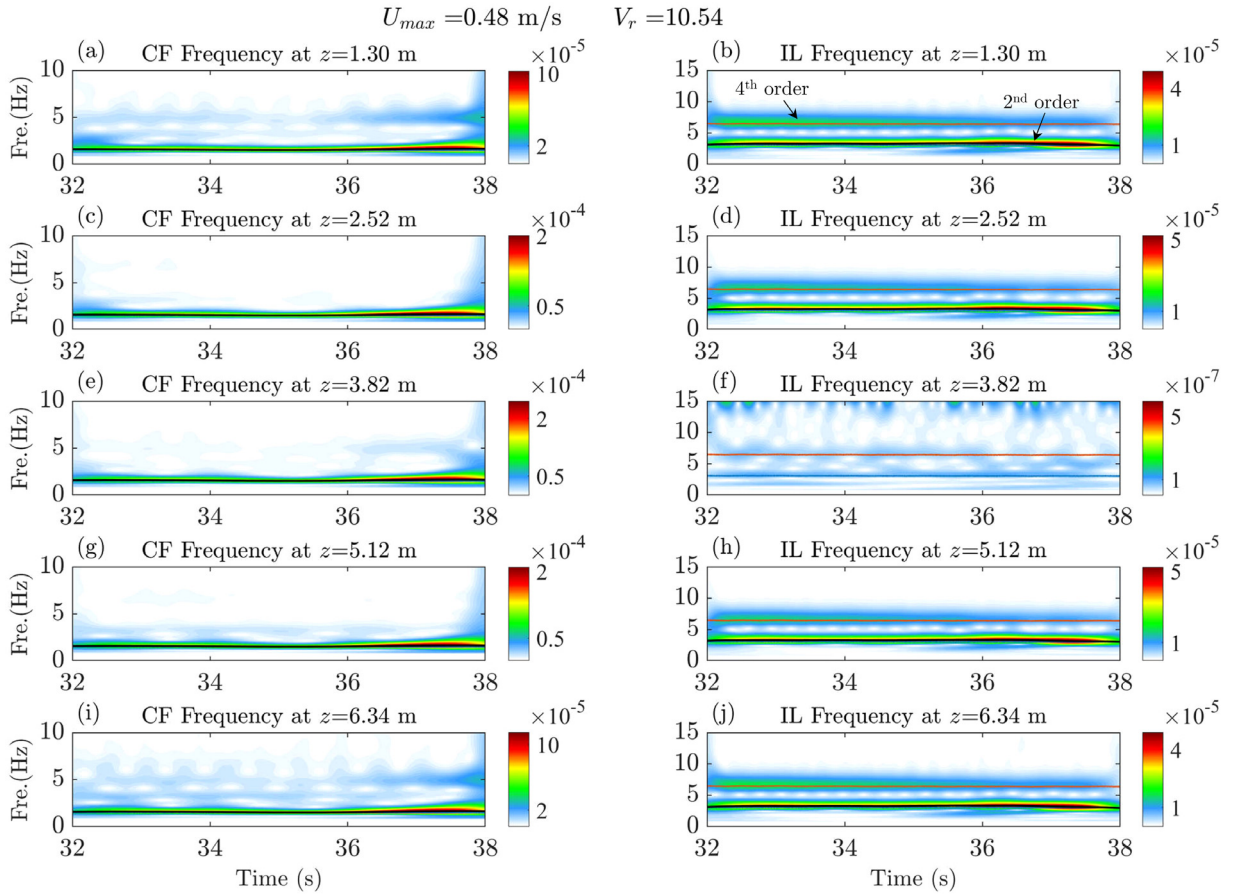
$U_{max} = 0.48$ m/s $V_r = 10.54$

Fig. 23. Time-varying response frequency for case $U_{max} = 0.48$ m/s, $Vr = 10.54$. a,c,e,g,i: time-varying CF response frequency at 5 selected probe points, the instantaneous natural frequency of the first three orders based on Eq. (1) are displayed; b,d,f,h,j: time-varying IL response frequency at 5 selected probe points. The instantaneous natural frequency of the selected orders based on Eq. (1) are shown. The black line represents the time-varying dominant frequency. (For interpretation of the references to color in this figure legend, the reader is referred to the web version of this article.)

5.2. Time–frequency analysis

Figs. 22 to 25 further demonstrate the time-varying response frequency distribution at 5 selected probe points under different test conditions. The flow profile and probe spots (solid red dots) are shown in the left sketch, and the time-varying response frequency based on wavelet transformation at different probe spots in the IL and CF directions is shown on the right. The color in the contour plots represents the instantaneous strength of the signal, and the dark red represents a stronger signal. The theoretical time-dependent natural frequencies at different orders based on the measured tension based on Eq. (1) are also shown. The contour plots of the wavelet transformation coefficient of VIV displacement at selected probe spots are shown in the figures.

Fig. 22 shows that the response frequency for case $U_{max} = 0.46$ m/s is consistent over time, the CF VIV is dominated by the 1st order (Fig. 22(a),(c),(e),(g) and (i)), and the IL VIV is dominated by the 1st order at the location away from the shift point of velocity direction with high current speed (Fig. 22(b),(d),(h) and (j)). The IL VIV at the location of the shift point of the velocity direction is dominated by the 3rd order (Fig. 22(f)). Fig. 23 shows that the CF VIV for case $U_{max} = 0.48$ m/s is dominated by the first order (Fig. 23(a),(c),(e),(g) and (i)), and the IL VIV exhibits a distinct and stable multi-mode behavior with the 2nd and 4th order (Fig. 23(b),(d),(f),(h) and (j)). The 'multi-frequency' response arises in the IL direction when the 'mono-frequency' response with the first order dominates the CF VIV at a low VIV-occurring flow velocity. When U_{max} reaches 0.87 m/s, the CF VIV at the edge probe spots with a high current speed reaches a stable 2nd order response (Fig. 24(a),(c),(g) and (i)), and the CF VIV at the middle probe spot with nearly zero flow velocity is still dominated by the 1st order containing a small 3rd order response component (Fig. 24(e)), where the 2nd order response does not occur as the flow velocity increases. The 3rd order response is excited at the ends of the pipe model with high flow velocity (Fig. 25(a) and (i)). The 2nd-order response is also excited at the probe points $z = 2.52$ and 5.12 m
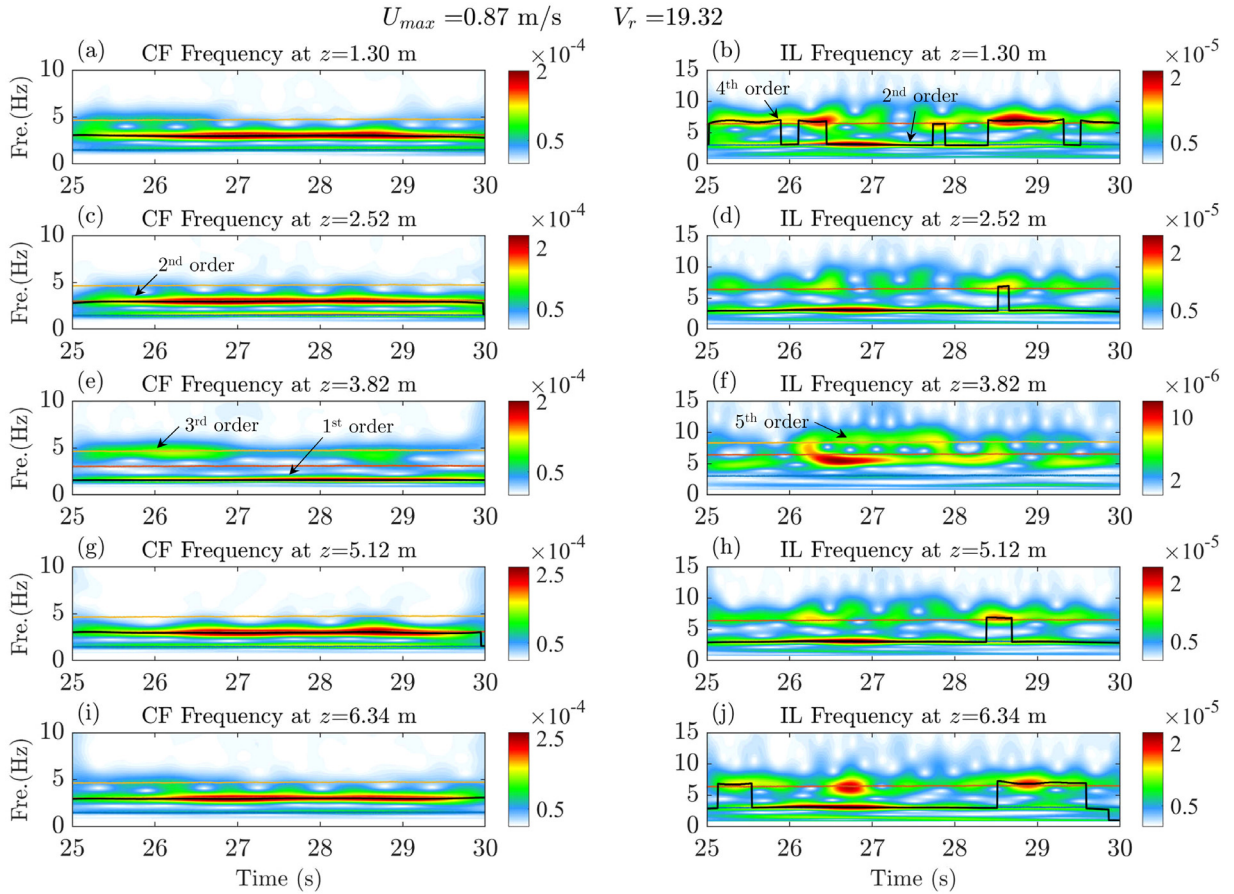
Fig. 24. Time-varying response frequency for case $U_{max} = 0.87$ m/s, $Vr = 19.32$. a,c,e,g,i: time-varying CF response frequency at 5 selected probe points, the instantaneous natural frequency of the first three orders based on Eq. (1) are displayed; b,d,f,h,j: time-varying IL response frequency at 5 selected probe points. The instantaneous natural frequency of the selected orders based on Eq. (1) are shown. The black line represents the time-varying dominant frequency. (For interpretation of the references to color in this figure legend, the reader is referred to the web version of this article.)

(Fig. 25(c) and (g)). The VIV response in the IL direction becomes more chaotic with an intermittent 5th order dominant frequency (Fig. 25(b),(d),(f),(h) and (j)).

An interesting question is whether the multi-frequency response under bidirectional sheared flow is instantaneously mono-frequency with a shifting frequency in the time domain, which is also called 'time-sharing' (Swithenbank and Larsen, 2012), or is multi-frequency at all times. From the results of the wavelet transform shown in Figs. 23 to 25, we can infer that only one predominant frequency with small deviations exists in the time domain in the mono-frequency case (Fig. 23). Regarding the multi-frequency cases (Figs. 24 and 25), an instantaneous broad frequency response does not exist, but an instantaneous single frequency that shifts from one predominant frequency to another does exist, as verified in the CF direction (Fig. 24(b) and Fig. 25(i)). The response frequency in the IL direction is noisier and more chaotic (Fig. 25(f)), and the 'time-sharing' is less pronounced compared to the CF direction. In some test conditions (Figs. 24(b),(j); 25(f)), there exist 'multi-frequency' vibration characteristic. Overall, it can be considered that 'time-sharing' also occurs in the CF direction under bidirectionally sheared flow induced VIV, and the 'multi-frequency' characteristic is more obvious in the IL direction.

The spatial and temporal distributions of the VIV displacement along the pipe span for different cases are shown from Figs. 26 to 29 which explain the instability of wavelet analysis. The color of the figures demonstrates the instantaneous normalized VIV amplitude. The red contours indicate a positive amplitude, while blue contours indicate a negative amplitude. Black arrows indicate the traveling wave phenomenon.

Fig. 26 shows the VIV response at $U_{max} = 0.46$ m/s, while the IL response demonstrates the traveling wave phenomenon at a low flow velocity. Even in the lowest flow velocity case, where the highest CF VIV response is approximately $0.05D$, which can be termed VIV does not occur apparently, the traveling wave phenomenon still exists in the IL direction. Traveling waves can always occur in the IL direction. The VIV response at $U_{max} = 0.48$ m/s, as shown in Fig. 27, represents a standing wave pattern. The CF structural displacements are periodic and dominated by the 1st mode.
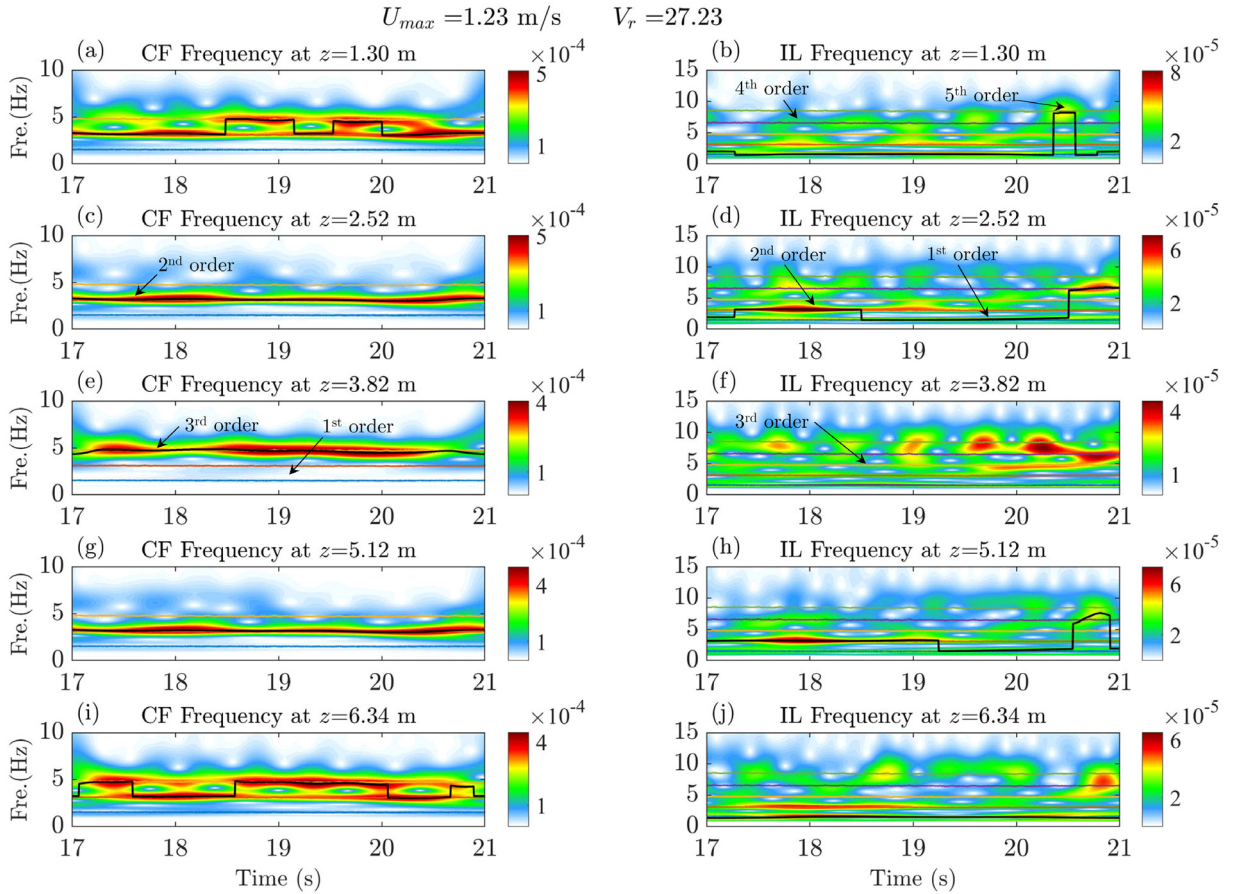
Fig. 25. Time-varying response frequency for case $U_{max} = 1.23$ m/s, $Vr = 27.23$. a,c,e,g,i: time-varying CF response frequency at 5 selected probe points, the instantaneous natural frequency of the first three orders based on Eq. (1) are displayed; b,d,f,h,j: time-varying IL response frequency at 5 selected probe points. The instantaneous natural frequency of the selected orders based on Eq. (1) are shown. The black line represents the time-varying dominant frequency. (For interpretation of the references to color in this figure legend, the reader is referred to the web version of this article.)

The IL structural displacements are dominated by the 1st and 2nd combining modes. Marked traveling wave patterns occur when the flow velocity increases, as shown in Figs. 28 and 29, which induce VIV instability in the time domain. These two figures indicate that the traveling wave pattern tends to spread from the high-velocity region toward the low-velocity region. The traveling wave under the bidirectionally sheared flow propagates from one end to the other end with reverse velocity and does not reflect from the turning point of the flow velocity.

5.3. Phase analysis

In this section, the phase analysis (synchronization) between IL and CF VIV (Bourguet et al., 2011; Huera-Huarte and Bearman, 2009; Pikovsky et al., 2003) is applied. The phase difference between in-line and cross-flow VIV of the cylinder is used to quantify the synchronization phenomenon which is shown to be related to the nature of the fluid–structure energy transfer (Huera-Huarte and Bearman, 2009). The instantaneous phases of IL and CF VIV (ϕ_x and ϕ_y) are obtained by the Hilbert transform. The phase difference ϕ_{xy} in the previous research is defined as:

$$\phi_{xy}(z, t) = \left[p\phi_x(z, t) - q\phi_y(z, t), \quad \mod 360° \right] \tag{18}$$

where p and q are set equal to 1 and 2, respectively, for linearly sheared flow. However, in bidirectionally sheared flow, the dominant frequency varies along the cylinder. Fig. 30 represents the distribution of dominant frequencies in the CF and IL directions at $U_{max} = 1.23$ m/s. Black circles represent the dominant frequencies of displacement at different spanwise locations, and results show that the ratio of frequencies in the CF and IL directions is not consistent along the cylinder in bidirectionally sheared flow.
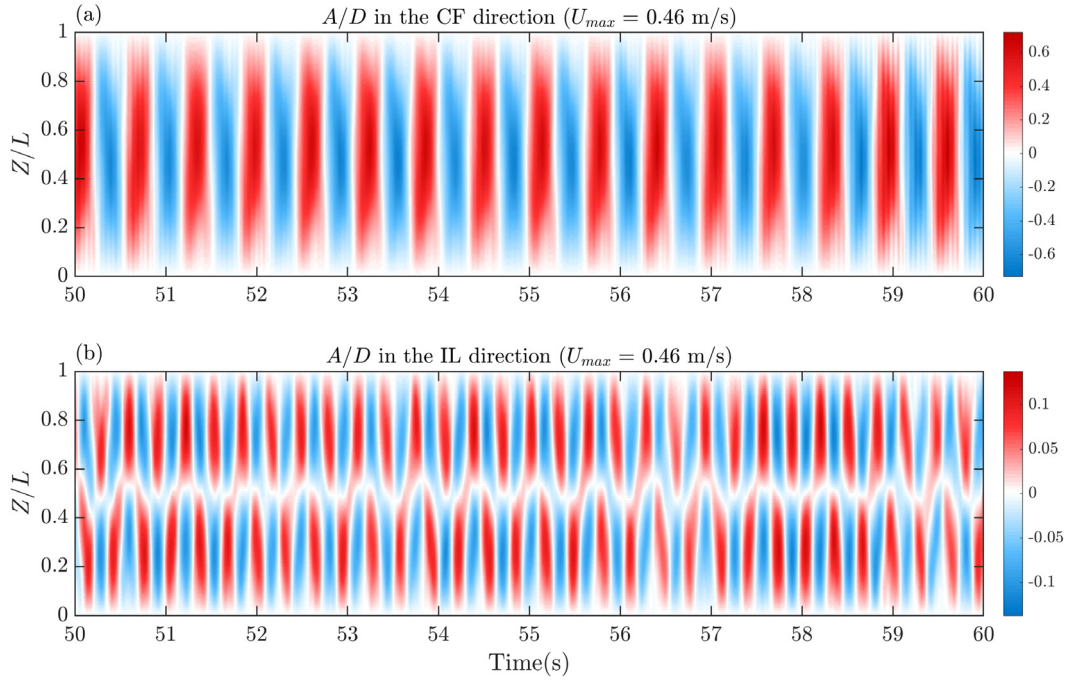
Fig. 26. Spatial and temporal distributions of the VIV displacement along the pipe span for case $U_{max} = 0.46$ m/s: (a) nondimensional VIV displacement (A/D) in the CF direction; (b) nondimensional VIV displacement (A/D) in the IL direction. (For interpretation of the references to color in this figure legend, the reader is referred to the web version of this article.)
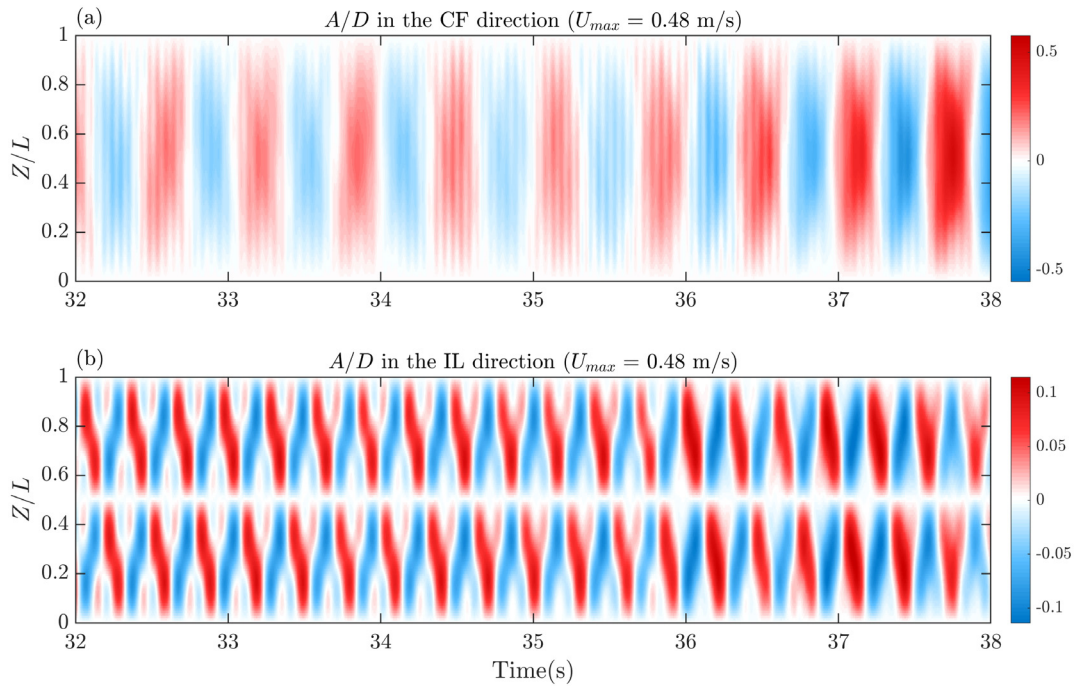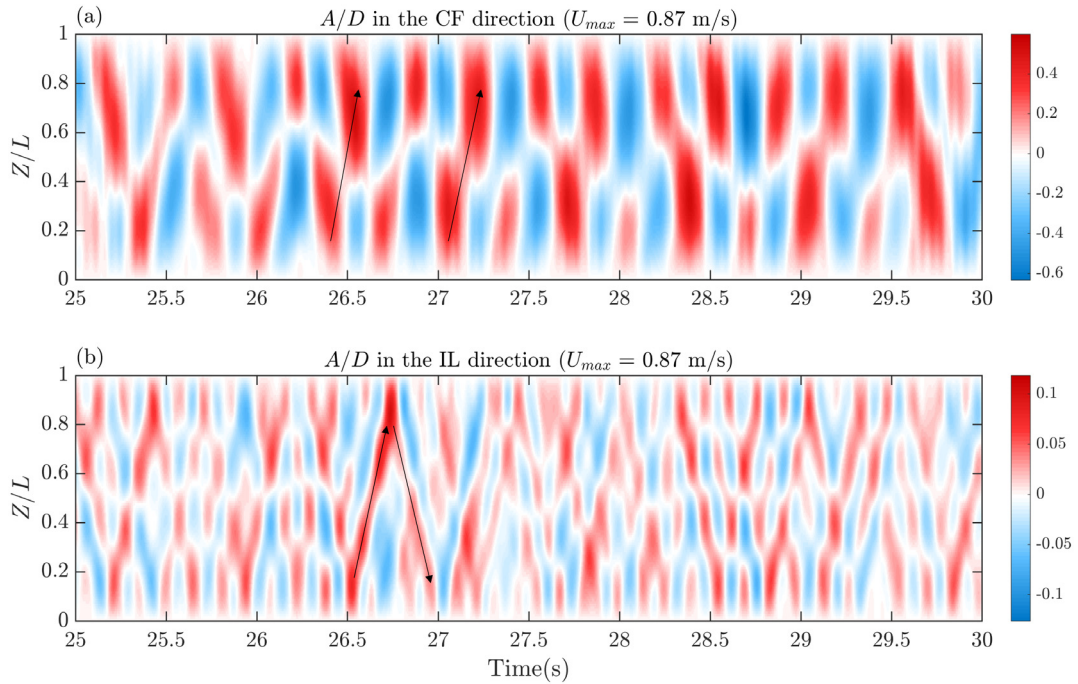

Fig. 27. Spatial and temporal distributions of the VIV displacement along the pipe span for case $U_{max} = 0.48$ m/s: (a) nondimensional VIV displacement (A/D) in the CF direction; (b) nondimensional VIV displacement (A/D) in the IL direction. (For interpretation of the references to color in this figure legend, the reader is referred to the web version of this article.)

Fig. 28. Spatial and temporal distributions of the VIV displacement along the pipe span for case $U_{max} = 0.87$ m/s: (a) nondimensional VIV displacement (A/D) in the CF direction; (b) nondimensional VIV displacement (A/D) in the IL direction. The arrow indicates the direction of traveling wave. (For interpretation of the references to color in this figure legend, the reader is referred to the web version of this article.)
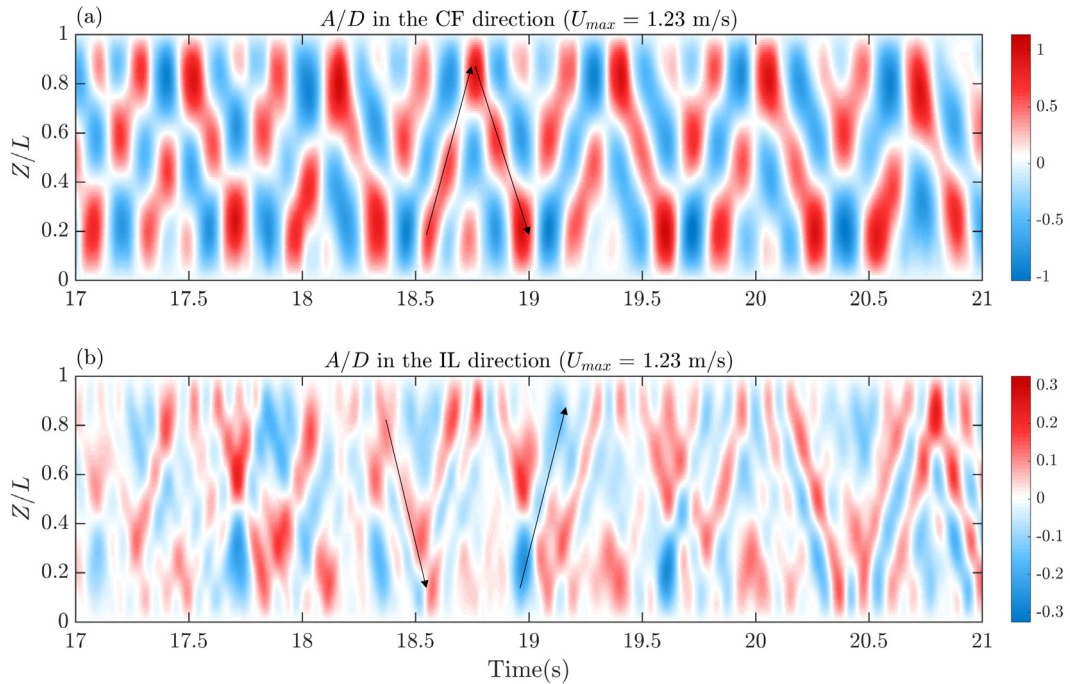

Fig. 29. Spatial and temporal distributions of the VIV displacement along the pipe span for case $U_{max} = 1.23$ m/s: (a) nondimensional VIV displacement (A/D) in the CF direction; (b) nondimensional VIV displacement (A/D) in the IL direction. The arrow indicates the direction of traveling wave. (For interpretation of the references to color in this figure legend, the reader is referred to the web version of this article.)
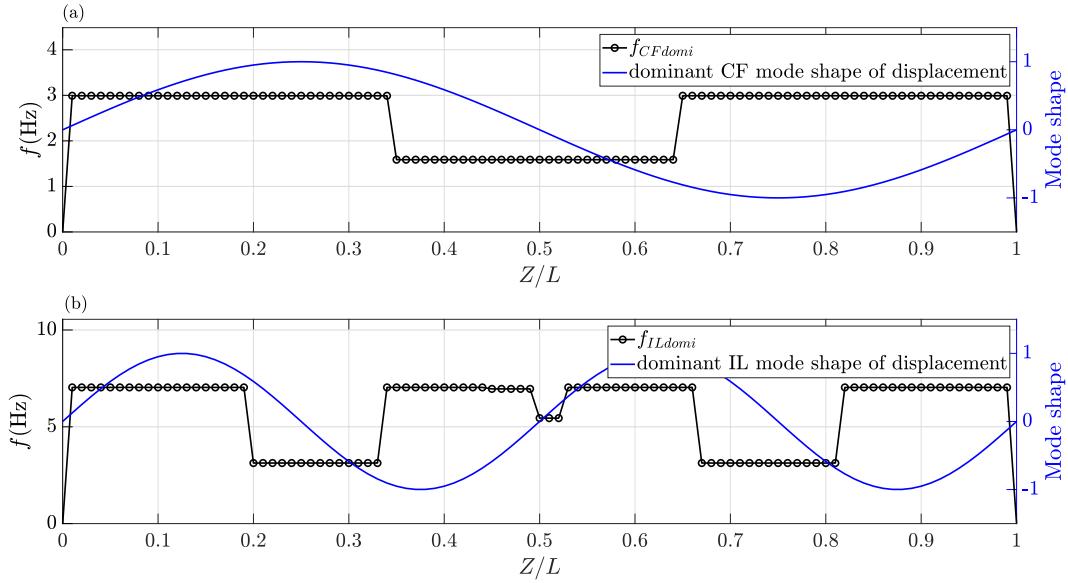
Fig. 30. Spanwise distribution of dominant frequency for case $U_{max} = 0.87$ m/s: (a) CF direction; (b) IL direction.
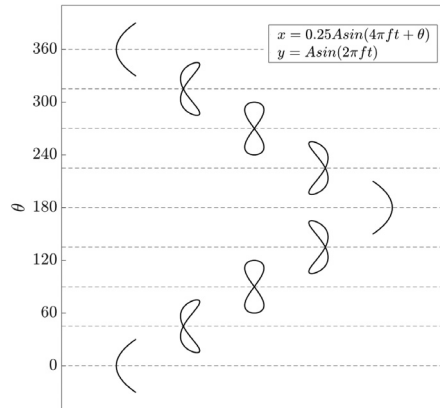

Fig. 31. Trajectories at different phase differences (x and y represents the IL and CF directions, respectively).

Therefore, the phase difference ϕ_{xy} in this study is determined by following:

$$\phi_{xy}(z,t) = \left[\phi_x(z,t) - \frac{f_x(z,t)}{f_y(z,t)}\phi_y(z,t), \quad \mod 360° \right] \tag{19}$$

where $f_x(z,t)$ and $f_x(z,t)$ are the instantaneous dominant response frequencies at different spanwise locations obtained from the max values of wavelet transformation results shown in the previous chapter and include the effect of changes in the dominant frequency along with the cylinder.

The phase difference value is directly reflected in the VIV trajectory. The ranges $0° \sim 180°$ and $180° \sim 360°$ represents a 'counter-clockwise' and 'clockwise' trajectory, respectively. Fig. 31 shows typical trajectories with different phase differences. Flow direction and motion direction are omitted.

Spatial and temporal distributions of the phase difference between IL and CF displacements under selected test conditions are shown in Fig. 32. When $U_{max} = 0.46$ m/s, the phase difference is essentially consistent along the span except for the zone around the turning point of the flow direction and ends. The phase difference there is unstable through the temporal domain, as shown by the black box in the figure. In addition, the unsteadiness of the phase difference at sections increases with U_{max}.

The phase difference in the time domain along the cylinder is quite unsteady, and histogram analysis is used to determine the predominant phase difference along the span. The histograms of ϕ_{xy} are evaluated from the time series shown in Fig. 32. Fig. 33 shows the histogram results of different test conditions along with the cylinder (contour plot of the normalized contribution).
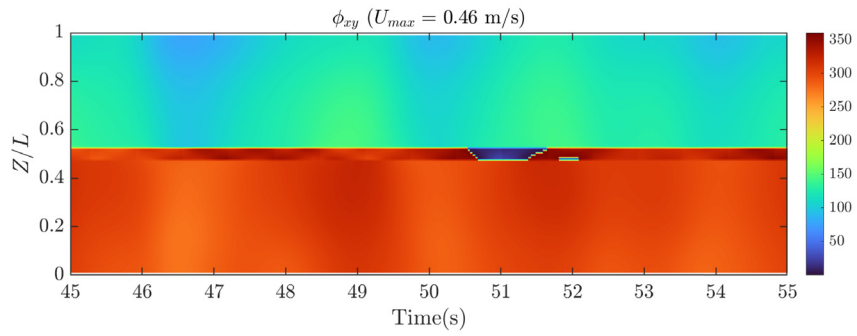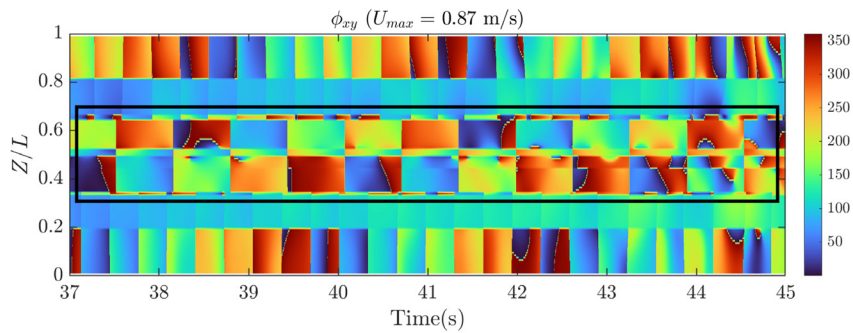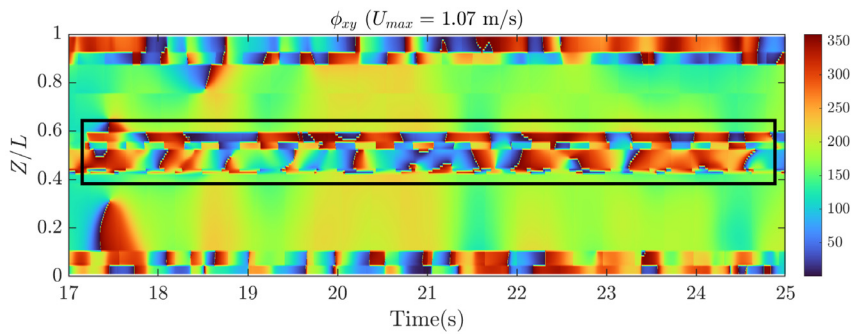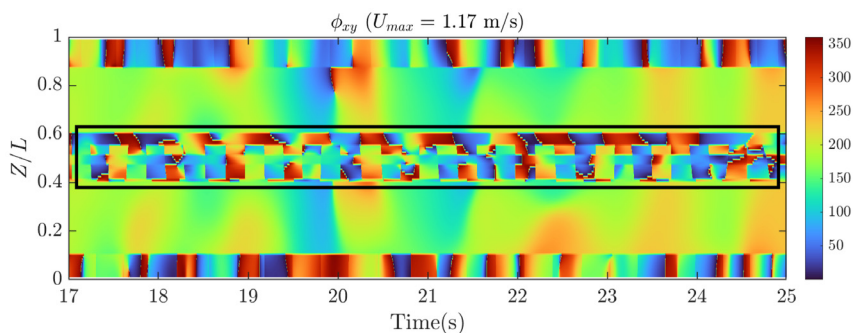
Fig. 32. Spatial and temporal distribution of the phase difference between IL and CF displacements along the cylinder span at (a) $U_{max} = 0.46$ m/s, (b) $U_{max} = 0.87$ m/s, (c) $U_{max} = 1.07$ m/s and (d) $U_{max} = 1.17$ m/s.

Fig. 33. Histogram results of phase difference at (a) $U_{max} = 0.46\,\text{m/s}$, (b) $U_{max} = 0.87\,\text{m/s}$, (c) $U_{max} = 1.07\,\text{m/s}$ and (d) $U_{max} = 1.17\,\text{m/s}$.
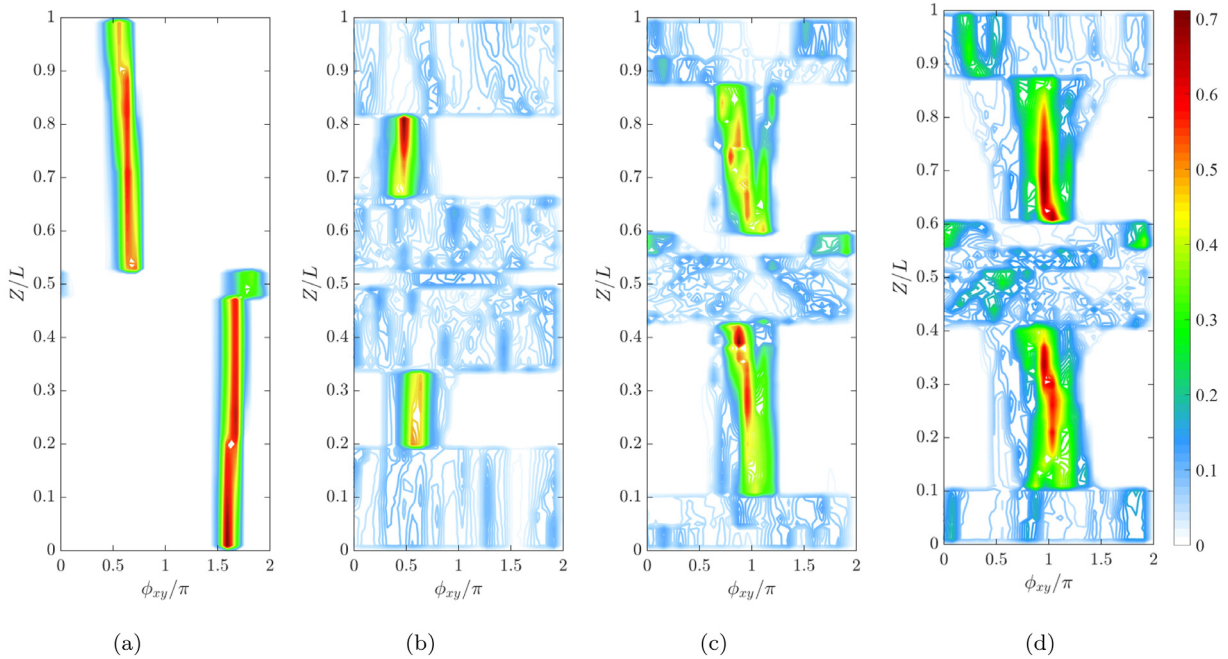
With $U_{max} = 0.46\,\text{m/s}$ (Fig. 33(a)), there are two regions of phase difference: $0.00L < Z < 0.50L$, and $0.50L < Z < 1.00L$. The magnitude of the phase difference remains relatively constant in the half-length and exists a jump of π (180 degrees) at the IL node location ($Z/L \approx 0.5$). The phase difference of each region is nearly constantly induced by the standing wave dominant VIV, and a jump of π (180 degrees) exists at the IL node location ($Z/L \approx 0.5$) due to the symmetrically distributed flow field. The phase differences of cases $U_{max} = 0.87$, 1.07 and 1.17 m/s shown in Fig. 33(b),(c) and (d) show similar patterns. Symmetric synchronization and non-synchronization regions exist. The synchronization region is located in the middle of the flow field in the same direction of flow, ranging by approximately half from $0.1L$ to $0.4L$. The symmetric flow profile makes the synchronization regions distributed symmetrically. The non-synchronization region is located near the changeover point of the velocity direction and the ends. As the flow rate increases, the range of the synchronization area gradually increases. The largest synchronization region observed in the experiment is approximately $[0.1L : 0.4L] \cup [0.6L : 0.9L]$. Different from the standing wave dominant VIV, no phase jump exists between the synchronization regions in these test conditions due to the traveling wave pattern.

Fig. 34 shows the VIV state of the test pipe under selected cases. Black lines represent the initial displacement in the IL direction, and gray lines represent trajectories of selected locations ($Z/L = 0.25, 0.50, 0.75$). As analyzed previously, the phase differences become more chaotic as the flow velocity increases, which is reflected directly in the trajectory results. The 2D VIV trajectories under small flow velocities, such as the case of $U_{max} = 0.46\,\text{m/s}$, show clear figures of eight and the 2nd order mode at $Z/L = 0.25$ and 0.50, respectively. Trajectories at symmetrical positions present symmetrical phases as shown in Fig. 34(a). As the flow velocity increases, the trajectories become more irregular (Fig. 34(b), (c) and (d)).

6. Summary

We performed an experiment with a flexible pipe that was 28.41 mm in diameter and 269 diameters in length under bidirectionally sheared flow to analyze its response characteristics. The bending strain of VIV was measured in the CF and IL directions at 9 and 14 locations, respectively. A verified modal analysis method was then used to determine the VIV displacement from the strain signals. A total of 58 test conditions with maximum flow velocities varying from 0.30 to 1.39 m/s were used in this experiment.

The RMS VIV response in the CF and IL directions reached maximum levels of $0.51D$ and $0.18D$, respectively. In addition to the ubiquitous '2n/n' and '2n/2n-1' modal groups, modal groups '3/1' and '4/1' existed under low flow velocity, in which the IL VIV reached a higher mode response under the slow flow velocity due to the special flow profile.

The Strouhal numbers under the bidirectional sheared flow were approximately 0.10 and 0.24 in the CF and IL directions, respectively, which were smaller than the St numbers under uniform flow and linearly sheared flow. These results indicated that the bidirectionally sheared flow caused a lower response frequency.
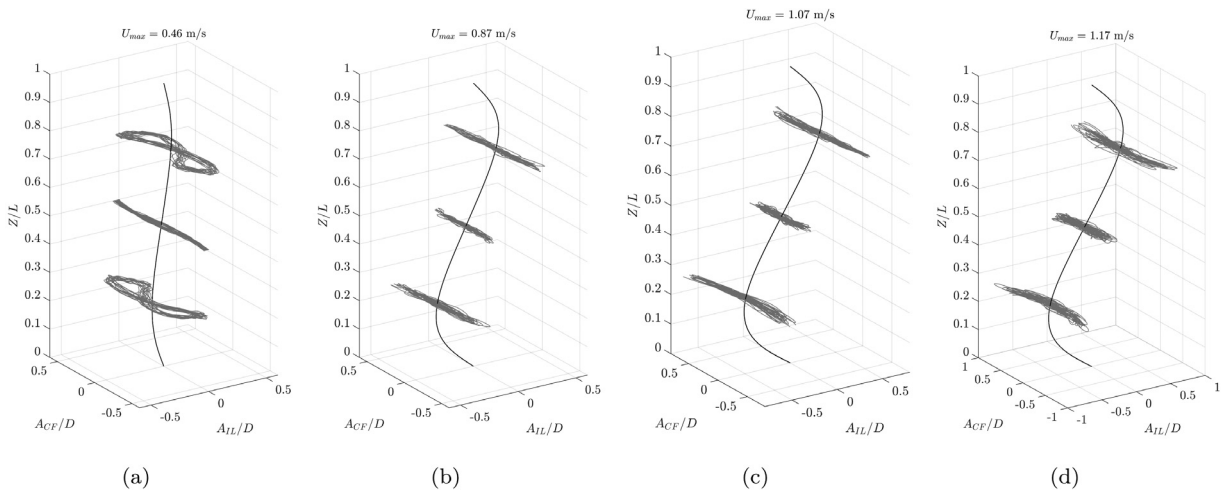
Fig. 34. VIV state of test pipe of different cases. black line: initial IL displacement; gray line: 2D trajectories at different locations ($Z/L = 0.25, 0.50, 0.75$). The displacement is nondimensionalized by the diameter D : (a) $U_{max} = 0.46\,\text{m/s}$, (b) $U_{max} = 0.87\,\text{m/s}$, (c) $U_{max} = 1.07\,\text{m/s}$ and (d) $U_{max} = 1.17\,\text{m/s}$.

A strong traveling wave and 'multi-frequency' response phenomenon were also found, particularly in the IL directions, which made the phase difference of IL and CF VIV displacements unstable in the time domain. When the maximum flow velocity was small, VIV was dominated by the standing wave response, and a jump in the phase difference occurred at the IL node location. As the flow velocity increased, two symmetrical phase synchronization regions existed.

CRediT authorship contribution statement

Xuepeng Fu: Conceptualization, Methodology, Investigation, Validation, Writing – original draft. **Shixiao Fu:** Conceptualization, Methodology, Investigation, Writing – review & editing, Supervision. **Haojie Ren:** Investigation, Writing – review & editing. **Wenhui Xie:** Writing – review & editing. **Yuwang Xu:** Investigation, Writing – review & editing. **Mengmeng Zhang:** Investigation, Writing – review & editing. **Zhenhui Liu:** Writing – review & editing. **Shuai Meng:** Writing – review & editing.

Declaration of competing interest

The authors declare that they have no known competing financial interests or personal relationships that could have appeared to influence the work reported in this paper.

Data availability

The data that has been used is confidential.

Acknowledgments

References

Bourguet, R., Karniadakis, G.E., Triantafyllou, M.S., 2011. Vortex-induced vibrations of a long flexible cylinder in shear flow. J. Fluid Mech. 677, 342–382.

Chaplin, J., Bearman, P., Cheng, Y., Fontaine, E., Graham, J., Herfjord, K., Huarte, F.H., Isherwood, M., Lambrakos, K., Larsen, C., et al., 2005a. Blind predictions of laboratory measurements of vortex-induced vibrations of a tension riser. J. Fluids Struct. 21 (1), 25–40.

Chaplin, J., Bearman, P., Huarte, F.H., Pattenden, R., 2005b. Laboratory measurements of vortex-induced vibrations of a vertical tension riser in a stepped current. J. Fluids Struct. 21 (1), 3–24.

Gao, Y., Fu, S., Ren, T., Xiong, Y., Song, L., 2015. VIV response of a long flexible riser fitted with strakes in uniform and linearly sheared currents. Appl. Ocean Res. 52, 102–114.

Govardhan, R., Williamson, C., 2000. Modes of vortex formation and frequency response of a freely vibrating cylinder. J. Fluid Mech. 420, 85–130.

Huera-Huarte, F., 2006. Multi-Mode Vortex-Induced Vibrations of a Flexible Circular Cylinder (Ph.D. thesis). Imperical College London.

Huera-Huarte, F., Bearman, P., 2009. Wake structures and vortex-induced vibrations of a long flexible cylinder—part 1: dynamic response. J. Fluids Struct. 25 (6), 969–990.

Jauvtis Na, Williamson, C., 2004. The effect of two degrees of freedom on vortex-induced vibration at low mass and damping. J. Fluid Mech. 509, 23–62.

Larsen, C.M., Vikestad, K., Yttervik, R., Passano, E., Baarholm, G., 2001. VIVANA Theory Manual. Marintek, Trondheim, Norway.

Lie, H., Kaasen, K., 2006. Modal analysis of measurements from a large-scale VIV model test of a riser in linearly sheared flow. J. Fluids Struct. 22 (4), 557–575.

Pikovsky, A., Rosenblum, M., Kurths, J., Strogatz, S., 2003. Books-synchronization: A universal concept in nonlinear sciences. Phys. Today 56 (1), 47.

Ren, H., Xu, Y., Cheng, J., Cao, P., Zhang, M., Fu, S., Zhu, Z., 2019. Vortex-induced vibration of flexible pipe fitted with helical strakes in oscillatory flow. Ocean Eng. 189, 106274.

Sarpkaya, T., 2004. A critical review of the intrinsic nature of vortex-induced vibrations. J. Fluids Struct. 19 (4), 389–447.

Swithenbank, S.B., Larsen, C.M., 2012. Occurrence of high amplitude VIV with time sharing. In: International Conference on Offshore Mechanics and Arctic Engineering, Vol. 44922. American Society of Mechanical Engineers, pp. 723–729.

Swithenbank, S.B., Vandiver, J.K., Larsen, C.M., Lie, H., 2008. Reynolds number dependence of flexible cylinder VIV response data. In: International Conference on Offshore Mechanics and Arctic Engineering, Vol. 48227. pp. 503–511.

Tognarelli, M., Slocum, S., Frank, W., Campbell, R., 2004. VIV response of a long flexible cylinder in uniform and linearly sheared currents. In: Offshore Technology Conference. OnePetro.

Triantafyllou, M., Triantafyllou, G., Tein, Y., Ambrose, B.D., 1999. Pragmatic riser VIV analysis. In: Offshore Technology Conference. OnePetro.

Trim, A., Braaten, H., Lie, H., Tognarelli, M., 2005. Experimental investigation of vortex-induced vibration of long marine risers. J. Fluids Struct. 21 (3), 335–361.

Vandiver, J.K., 1993. Dimensionless parameters important to the prediction of vortex-induced vibration of long, flexible cylinders in ocean currents. J. Fluids Struct. 7 (5), 423–455.

Vandiver, J., Lee, L., Leverette, S., Marcollo, H., 2005. User guide for SHEAR7 version 4.4.

Vikestad, K., Larsen, C.M., Vandiver, J.K., 2000. Norwegian deepwater program: damping of vortex-induced vibrations. In: Offshore Technology Conference. OnePetro.

Wang, Z., Fan, D., Triantafyllou, M.S., Karniadakis, G.E., 2021. A large-eddy simulation study on the similarity between free vibrations of a flexible cylinder and forced vibrations of a rigid cylinder. J. Fluids Struct. 101, 103223.

Wang, J., Fu, S., Baarholm, R., Wu, J., Larsen, C.M., 2014. Fatigue damage of a steel catenary riser from vortex-induced vibration caused by vessel motions. Mar. Struct. 39, 131–156.

Willden, R., Graham, J., 2001. Numerical prediction of VIV on long flexible circular cylinders. J. Fluids Struct. 15 (3–4), 659–669.

Williamson, C.H., Govardhan, R., 2004. Vortex-induced vibrations. Annu. Rev. Fluid Mech. 36, 413–455.

Williamson, C., Govardhan, R., 2008. A brief review of recent results in vortex-induced vibrations. J. Wind Eng. Ind. Aerodyn. 96 (6–7), 713–735.

Williamson, C.H., Roshko, A., 1988. Vortex formation in the wake of an oscillating cylinder. J. Fluids Struct. 2 (4), 355–381.

Wu, X., Ge, F., Hong, Y., 2012. A review of recent studies on vortex-induced vibrations of long slender cylinders. J. Fluids Struct. 28, 292–308.

Xie, B., Lei, F., 2013. Characteristics of Internal Solitons at Liuhua Area in the South China Sea, Vol. 54. Shipbuilding of China, Special 2.

Xie, B.-T., Li, J.-g., Ren, X.-h., Lei, F.-h., 2018. The characteristic analysis of internal solitons in the Liuhua area of the South China Sea. In: The 28th International Ocean and Polar Engineering Conference. OnePetro.